Impacts of Secondary Ice Production on Arctic Mixed-Phase Clouds based on ARM Observations and CAM6 Single-Column Model Simulations

Xi Zhao[1], Xiaohong Liu[1], Vaughan T. J. Phillips[2], and Sachin Patade[2]

[1]Department of Atmospheric Sciences, Texas A&M University, College Station, Texas, 77840, USA

[2]Department of Physical Geography and Ecosystem Science, Lund University, Lund, Sweden

Correspondence to: Xiaohong Liu (xiaohong.liu@tamu.edu)

Abstract. For decades, measured ice crystal number concentrations have been found to be orders of magnitude higher than measured ice nucleating particle number concentrations in moderately cold clouds. This observed discrepancy reveals the existence of secondary ice production (SIP) in addition to the primary ice nucleation. However, the importance of SIP relative to primary ice nucleation remains highly unclear. Furthermore, most weather and climate models do not represent well the SIP processes, leading to large biases in simulated cloud properties. This study demonstrates a first attempt to represent different SIP mechanisms (frozen raindrop shattering, ice-ice collisional break-up, and rime splintering) in a global climate model (GCM). The model is run in the single column mode to facilitate comparisons with the Department of Energy (DOE)'s

19   Atmospheric Radiation Measurement (ARM) Mixed-Phase Arctic Cloud Experiment (M-PACE)

20   observations.

21   We show the SIP importance in the four types of clouds during M-PACE (i.e., multilayer clouds,

22   single-layer stratus, transition and frontal clouds), with the maximum enhancement in ice crystal

23   number concentrations by up to 4 orders of magnitude in moderately supercooled clouds. We reveal

24   that SIP is the dominant source of ice crystals near the cloud base for the long-lived Arctic single-

25   layer mixed-phase clouds. The model with SIP improves the occurrence and phase partitioning of

26   the mixed-phase clouds, reverses the vertical distribution pattern of ice number concentrations, and

27   provides a better agreement with observations. The findings of this study highlight the importance

28   of considering the SIP in GCMs.

1 Introduction

Clouds play a critical role in the surface energy budget of the Arctic, thereby affecting the Arctic sea ice and regional climate (Kay et al., 2009; Bennartz et al., 2013). Clouds occur frequently in the Arctic (Beaufort Sea) with an observed annual mean occurrence of 85%, a maximum of 97% in September, and a minimum of 63% in February (Intrieri et al., 2002). Along with the occurrence frequency, the phase partitioning between liquid and ice in mixed-phase clouds, i.e., the clouds where liquid and ice coexist at subfreezing temperatures, is also important, since even a small amount of liquid content in clouds can substantially change the radiative properties of the cloud (Shupe et al., 2004; Cesana and Chepfer, 2013). Shupe et al. (2006) showed that over the Beaufort Sea, 59% of observed clouds were mixed-phase, while another study indicated 90% over the western Arctic Basin (Pinto, 1998). Cloud properties further play a key role in the Arctic climate change through cloud feedbacks (Vavrus, 2004; Zhang et al., 2018; Tan and Storelvmo, 2019).

Mixed-phase clouds are microphysically unstable. Even a small amount of cloud ice can glaciate the mixed-phase clouds in a few hours via the Wegener–Bergeron–Findeisen (WBF) mechanism (Morrison et al., 2012). Mixed-phase clouds in the Arctic are long-lived and characterized by a structure with liquid water at the cloud top and ice water underneath. Interaction and feedback among multiple processes, including longwave

50 radiative cooling, turbulence entrainment, and condensation of liquid water, provide

51 sufficient moistening and cooling at the cloud top. This sustains enough formation of liquid

52 mass against the depletion by the WBF process. In order to support the self-maintenance

53 of liquid water, low concentrations of small ice particles must be present near the cloud

54 base (Shupe et al., 2006; Korolev and Field, 2008). In this way, they are efficient in

55 sedimentation (Jiang et al., 2000) but less active in the WBF and vapor deposition

56 processes. Previous studies indicated that 90% of Arctic mixed-phase cloud temperatures

57 were between -25°C and -5°C from an annual mean perspective (Shupe et al., 2006),

58 indicating that ice exists in moderately supercooled clouds. However, the mechanisms

59 contributing to ice formation in these clouds are still unclear (Shupe et al., 2006; Morrison

60 et al., 2012). One objective of this study is to better understand the ice formation processes

61 in the Arctic mixed-phase clouds.

62   Previous studies have shown the important role of SIP in the Arctic clouds from

63 observations (Schwarzenboeck et al., 2009) and small-scale model simulations

64 (Sotiropoulou et al., 2020a; Fu et al., 2019). Using a large-eddy simulation (LES) model

65 and a Lagrangian parcel model, Sotiropoulou et al. (2020a) found that a combination of

66 ice-ice collisional fragmentation and rime splintering provides a better agreement of the

67 simulated ice crystal number concentrations (ICNCs) with observations in the summer

68 Arctic stratocumulus. They found a low sensitivity of SIP to prescribed number

69 concentrations of cloud condensation nuclei (CCN) and ice nucleating particles (INPs). Fu

70   et al. (2019) simulated an autumnal Arctic single-layer boundary-layer mixed-phase cloud

71   using the Weather Research and Forecasting (WRF) model and showed that the model

72   without considering SIP needs an increase of INP concentrations by two orders of

73   magnitude to match the observed ICNCs. In comparison, the model that only considers the

74   SIP through droplet shattering needs an INP increase of 50 times to match the observed

75   ICNCs.

76   The roles of SIP have also been investigated in other geographical regions and for

77   other cloud types. Sotiropoulou et al. (2020b) simulated a summer boundary layer coastal

78   cloud in West Antarctica using the WRF model and found that the model with collisional

79   break-up between ice-phase particles can reproduce the observed ICNCs, which could not

80   be explained by the rime splintering or primary ice nucleation. Sullivan et al. (2017) used

81   a parcel model with rime splintering and graupel-graupel collisional break-up and found

82   that these two SIP processes can enhance the ICNCs by four orders of magnitude. Sullivan

83   et al. (2018a) showed that among the different SIP mechanisms, only ice–ice collisional

84   fragmentation contributes to a meaningful ice enhancement (larger than $0.002 \ \mathrm{L}^{-1}$) in a

85   parcel model simulation. Other studies have shown the impact of SIP on ICNCs in a cold

86   frontal rain band over the UK (Sullivan et al., 2018b), on surface precipitation of a tropical

87   thunderstorm (Connolly et al., 2006), and on the summertime cyclones (Dearden et al.,

88   2016).

89   Previous modeling studies have used small-scale (e.g., parcel models and LES

90   models) and regional-scale models, to investigate the impacts of SIP on cloud properties.

91   There is still a lack of large-scale perspective based on global climate models (GCMs).

92   Moreover, the mechanisms contributing to ice production in the Arctic mixed-phase clouds

93   at moderately cold temperatures are still unknown. In this study, for the first time, we

94   implemented the representation of two new SIP mechanisms (i.e., raindrop shattering, ice-

95   ice collisional break-up) in a GCM. We tested the model performance by running the model

96   in the single column mode (SCM) and compared the SCM simulations of Arctic clouds

97   with observations. The objectives of this study are to examine the impact of SIP on different

98   types of the Arctic clouds and, ultimately to improve the model capability of representing

99   ice processes.

100   This paper is organized as follows. In section 2, we describe the GCM, associated

101   parameterizations, and the three SIP mechanisms represented in the model. In section 3,

102   we present the model experiments and observation data used for model evaluation. The

103   model results are presented in section 4. The main conclusions of this study and future

104   work are summarized in section 5.

2 Model and Parameterizations

2.1 Model description

The Community Atmosphere Model version 6 (CAM6) used in this study is the atmosphere component of the Community Earth System Model version 2 (CESM2). It includes multiple physical parameterizations that are related to ice formation and evolution. Cloud microphysics is described by a double-moment scheme (Gettelman and Morrison, 2015, hereafter as MG). The scheme considers homogeneous freezing of cloud droplets (with temperatures below –40 °C), heterogeneous freezing of cloud droplets, the WBF process, accretion of cloud droplets by snow, and the rime splintering. SIP from rime splintering is parameterized based on Cotton et al. (1986). The condensation process is also known as cloud macrophysics, which is governed by the Cloud Layers Unified by Binormals (CLUBB) scheme, assuming that all the condensate is in the liquid phase (Golaz et al., 2002; Larson et al., 2002). Furthermore, CLUBB also treats boundary layer turbulence and shallow convection. In the mixed-phase clouds, heterogeneous ice nucleation is represented by the classical nucleation theory (CNT), which relates ice nucleation rate to mineral dust and black carbon aerosols (Wang et al., 2014). In cirrus clouds, where temperatures are below –37 °C, heterogeneous immersion freezing on dust can compete with homogeneous freezing of sulfate (Liu and Penner, 2005). The aerosol species involved in ice nucleation processes are

123   represented by the four-mode version of the Modal Aerosol Module (MAM4) (Liu et al.,

124   2012; Liu et al., 2016).

125   In this study, we conducted the simulations using the SCM version of CAM6 (i.e.,

126   SCAM). SCAM is a one-column, time-dependent model configuration of CAM6 that

127   provides an efficient way to understand the behavior of model physical parameterizations

128   without the influence of nonlinear feedbacks from the large-scale circulation. In this way, the

129   biases of the modeled clouds can be exclusively identified from model evaluation against

130   observations.

131   **2.2 Implementation of secondary ice production in CESM2**

132   In addition to the existing SIP mechanism (i.e., rime splintering) in CAM6, we

133   implemented two new mechanisms of SIP, including ice-ice fragmentation and droplet

134   shattering (Phillips et al., 2017a, 2018) that are parameterized based on theoretical and

135   measurement research.

136   **a. An emulated bin framework**

137   Ideally, a bin microphysics scheme is the most suitable model setup for the

138   representation of SIP mechanisms in a model. However, running a GCM model with a bin

139   microphysics scheme is computationally too expensive under current computational

140   resources. To solve this problem, we developed an emulated bin framework for the existing

141   bulk MG microphysics scheme to facilitate the collisions of ice hydrometeors and

142   raindrops. First, we selected the bin bounds for each hydrometeor, including cloud ice,

143   snow, and rain. A logarithmically equidistant size grid is adopted, that is,

144
$$D_{k+1} = CD_k, \tag{1}$$

145   where $C = \sqrt[4]{2}$. The bin diameter ranges from 0.1 to 6 mm for raindrops and 0.1 to 50 mm

146   for snow and cloud ice particles. Based on the assumption of the particle size distribution,

147   the number concentration and mass mixing ratio of all hydrometeor types were calculated

148   in each temporary bin at each time step and grid point. The estimated particle size

149   distribution from the emulated bin framework served as inputs for the SIP schemes. The

150   SIP schemes were applied to each permutation of the bin during collisions of ice, snow,

151   and rain to calculate the secondary ice fragments. Finally, we summed up the fragment

152   from SIP over all pairs of bins.

153   The bin approach is only adopted in the SIP processes, while other processes,

154   including the existing collisions in the standard MG scheme, still use the bulk

155   microphysical approach. Thus, the modified MG scheme becomes a hybrid scheme that

156   combines the bulk and bin parameterizations. The advantage of this hybrid scheme is that

157   the scheme can provide an accurate representation of the SIP processes while still maintains

158   a relatively high computational efficiency, which is very important for GCMs. The hybrid

159   schemes have been widely used. For example, previous studies used the bin approach for

160   the warm rain processes, while adopted the bulk approach for the ice-related processes

161 (Onishi and Takahashi, 2012; Grabowski et al., 2010; Kuba and Murakami, 2010). Other

162 previous studies used the bin approach for the sedimentation (Morrison, 2012) or look-up

163 tables for the collision processes in the bulk schemes (Feingold et al., 1998).

164

165 **b. Ice-ice fragmentation**

166   Phillips et al. (2017a, b) developed a scheme for SIP during an ice-ice collision

167 based on the principle of energy conservation. This scheme relates the fragment numbers

168 to particle initial kinetic energy and ice particle habits (i.e., ice morphology), which can be

169 explained in terms of environmental temperature, particle size, and riming intensity of ice

170 particles (Fig. 1). The production of new ice particles per collision is calculated as:

171

172
$$\mathcal{N} \ = \ \alpha A \left[1 - e^{-\left(\frac{C k_0}{\alpha A}\right)^{\gamma}} \right] \tag{2}$$

173

174 in which α is the surface area of ice particle, i.e., the equivalent spherical area in a unit of

175 m^2, $\alpha = \pi D^2$; A is the number density of breakable asperities of ice particles, which is

176 related to riming intensity and ice particle size; C is the asperity-fragility coefficient,

177 prescribed to be 10815 for dendrites and 24780 for spatial planar; γ is a parameter related

178 to riming intensity (*rim*), $\gamma = 0.5 - (0.25 \times rim)$, and *rim* is assumed to be 0.1; k_0 is

179 the initial kinetic energy, which is given as:

180
$$k_0 = \frac{1}{2}\frac{m_1 m_2}{m_1 + m_2}(v_1 - v_2)^2 \qquad (3)$$

181   in which m_1 and m_2 are the particle masses of two colliding particles, and v_1 and v_2

182   are the terminal velocities of the two colliding particles.

183   In this method, three types of collision are identified based on the type of collision

184   particles: (1) cloud ice/snow collide with hail/graupel; (2) cloud ice/snow collide with

185   cloud ice/snow; (3) hail/graupel collide with hail/graupel (not included currently, since

186   CESM2-CAM6 does not treat graupel currently); For each collision type, different values

187   of parameters α, A, C, and γ in Eq. (2) are yielded based on the measured relationship

188   between fragment number and collisional kinetic energy (Phillips et al., 2017a).

189   Under the emulated bin framework, the new fragment production rate for each

190   permutation of a bin is written as:

191
$$N_{iic} = \mathcal{N}\, E_c \delta N_1 \delta N_2 \pi (r_1 + r_2)^2 |v_1 - v_2| \qquad (4)$$

192   in which E_c is the accretion efficiency, assumed to be 0.5 to be consistent with the MG

193   microphysics scheme, and δN_1 and δN_2 are the particle number concentrations in the

194   two bins with particle sizes of r_1 and r_2, respectively.

195   The ice production rate for cloud ice mixing ratio is:

196
$$P_{iic} = N_{iic}\delta m_{ice} \qquad (5)$$

197   in which δm_{ice} is mass for single ice particle, prescribed as 2.09×10^{-15} kg.

198 **c. Droplet shattering during rain freezing**

199   Phillips et al. (2018) proposed numerical formulations for ice multiplication during

200 the raindrop freezing. They suggested two modes of droplet break-up during the rain

201 freezing based on the relative weight of raindrop and ice particle (Fig. 2).

202   In mode 1, the freezing of rain is triggered by a collision with less massive ice

203 crystals or with INPs. By fitting to the laboratory data, Phillips et al. (2018) derived an

204 empirical formulation for the number of ice fragments per frozen raindrop as a function of

205 drop diameter and temperature. A Lorentzian distribution as a function of temperature was

206 adopted to represent the number of ice fragments per frozen raindrop. There are two types

207 of raindrop fragmentation: shattering to form "big" fragments and "tiny" splinters. The

208 total (big plus tiny) and big ice fragments per frozen raindrop emitted in the mode 1 of

209 droplet shattering are given in Eqs. (6) and (7), respectively:

210
$$\mathcal{N}_T = F(D)\Omega(T)\left[\frac{\zeta\eta^2}{(T-T_0)^2+\eta^2} + \beta T\right] \tag{6}$$

211
$$\mathcal{N}_B = min\left\{F(D)\Omega(T)\left[\frac{\zeta_B\eta_B^2}{(T-T_{B0})^2+\eta_B^2}\right], \mathcal{N}_T\right\} \tag{7}$$

212 where the parameters $\zeta, \eta, \beta, \zeta_B, \eta_B, T_0, T_{B0}$ are derived by fitting the formulations to a

213 collection of laboratory data. Further details about empirical formulae can be found in

214 Phillips et al. (2018). $F(D)$ and $\Omega(T)$ are the interpolating functions for the onset of

215 fragmentation and T is the temperature in K. The mass of a big fragment is $m_B = \chi_B m_{rain}$,

216   in which $\chi_B = 0.4$, and the mass of a small fragment is $m_S = \frac{\pi \rho_i}{6} D^3$, in which $\rho_i =$

217     $500 \, kg \, m^{-3}$.

218   The observational data used for the formulations of raindrop freezing by mode 1

219   was limited to drop diameter of 1.6 mm and a temperature range between –4 °C to –25 °C.

220   Phillips et al. (2018) linearly extrapolated their algorithm for larger particles and other

221   temperatures in the mixed-phase cloud regime. As shown in Fig. 2a, b, mode 1 of the

222   droplet shattering is most effective near -15°C.

223   In mode 2, a theoretical approach is adopted which is based on the assumption that

224   the number of fragments generated when a drop collides with a more massive ice particle

225   is controlled by the initial kinetic energy and surface energy (Fig. 2c). The number of

226   fragments generated per frozen drop in mode 2 is given as:

227             $$\mathcal{N}_{fr2} = 3\Phi(T) \times [1 - f(T)] \times \max{(DE - DE_c)}, \qquad (8)$$

228   where DE is the dimensionless energy and is expresses as:

229             $$DE = \frac{k_0}{S_e}, \qquad (9)$$

230   where k_0 is the initial kinetic energy which is given in Eq. (3), S_e is the surface energy,

231   expressed as $S_e = \gamma_{liq}\pi D^2$ (for D>150 μm), γ_{liq} is the surface tension of liquid water

232   which is 0.073 J m^{-2}. DE_c in Eq. (8) is set to be 0.2. $f(T)$ is the frozen fraction (Phillips

233   et al., 2018), and is given as:

234
$$f(T) = \frac{-C_w T}{L_f}.$$ (10)

235 where C_w is the specific heat capacity of liquid water (4200 J kg^{-1} K^{-1}) and L_f is the specific

236 latent heat of freezing (3.3×10^5 J kg^{-1}), $\Phi(T) = 0.5$ at $-1°C$ and $\Phi(T) = min\,[4f(T), 1]$.

d. Rime splintering

238   The MG microphysics already includes the SIP associated with rime splintering,

239 which is also known as Hallet-Mossop (HM) process. In this process, secondary ice

240 particles are generated during the accretion of cloud droplets by snow, and a part of rimed

241 mass is converted to cloud ice. The ice number production rate is based on the

242 parameterization of Cotton et al. (1986), which is given as:

243
$$N_{HM} = C_{sip\_HM} \times p_{sacws}$$ (11)

244 where p_{sacws} is the riming rate of cloud droplets by snow and is expressed as:

245
$$p_{sacws} = \frac{\pi \times a_{vs} \times \rho \times N_{0s} \times E_{ci} \times \Gamma(b_{vs}+3)}{4 \times \lambda^{b_{vs}+3}}$$ (12)

246 in which E_{ci} is the collection efficiency for the riming of cloud droplets by snow, a_{vs}

247 and b_{vs} are the fall speed parameters for snow particles, $b_{vs} = 0.41$, and $a_{vs} =$

248 $11.72 \times \frac{\rho_{850}}{\rho}$, ρ and ρ_{850} are air density and typical air density at 850 hPa, respectively,

249 and N_{0s} and λ are the parameters for the snow particle size distribution.

250   The conversion coefficient C_{sip_HM} in Equation (11) depends on temperature T_c in

251 ºC:

252
$$C_{sip\_HM} = \frac{3.5 \times 10^8 \times (-3-T)}{2}\ ,\ when\ -5 < T_c < -3,\ and$$ (13)

253 $$C_{sip\_HM} = \frac{3.5 \times 10^8 \times (T-(-8))}{3} \text{ , when } -8 < T_c < -5 \qquad (14)$$

254 The production rate for cloud ice mixing ratio is given as:

255 $$P_{HM} = N_{HM}\delta m_{ice} \qquad (15)$$

256 in which δm_{ice} is mass for single ice particle in the HM process, prescribed as 2.09×10^{-15}

257 kg. The rime splintering rate as a function of p_{sacws} and temperature is shown in Fig. 3.

3 Case Description, Observations, and Model Experiments

3.1 M-PACE case

260   In this study, we focus on the Arctic mixed-phase clouds observed during the

261 Department of Energy (DOE)'s Atmospheric Radiation Measurement (ARM) Mixed-

262 Phase Arctic Cloud Experiment (M-PACE). The M-PACE campaign was conducted over

263 the North Slope of Alaska (NSA) during the autumn from 27 September to 22 October 2004.

264   Various types of clouds were observed during M-PACE, including multilayer clouds,

265 boundary layer mixed-phase stratus, cirrus, and altostratus clouds associated with the frontal

266 system (Verlinde et al., 2007; Liu et al., 2007; Xie et al., 2008; Liu et al., 2011). Single-

267 layer mixed-phase clouds were formed under moderately supercooled conditions with the

268 cloud temperature at around –10 °C (Verlinde et al., 2007; McFarquhar et al., 2007),

269 providing a favorable condition for studying the influence of SIP on cloud evolution (Field

270 et al., 2016).

271   The synoptic-scale systems regulated the properties of clouds observed during the M-

272   PACE campaign. Hence, Verlinde et al. (2007) divided the M-PACE period into three

273   synoptic regimes and two transition periods based on the synoptic weather conditions. The

274   first synoptic regime began on 24 September and lasted until 1 October, 2004, when a well-

275   developed trough dominated aloft with several low-pressure systems that influenced the

276   surface. Followed by the first transition period between 2 and 3 October, the second synoptic

277   regime occurred between 4 and 14 October (Fig. 4), which was controlled by a pronounced

278   high-pressure system. The second transition period was from 15-17 October. By 18 October,

279   a fast-developing strong frontal system controlled the cloud formation over the NSA in the

280   third synoptic regime (Fig. 4). During M-PACE, the surface flux of water vapor, sensible

281   heat, and latent heat played different roles in the cloud formation. For example, clouds

282   formed in response to a strong surface forcing during the second regime, while clouds formed

283   under a relatively weak surface forcing during the third regime. In this study, we evaluate the

284   modeled cloud properties with M-PACE observations in the second and third synoptic

285   regimes focusing on the boundary layer mixed-phase stratus during 9-12 October in the

286   second regime.

287   **3.2 Observation data**

288   The observed cloud occurrence data at Barrow (located at 71.3° N, 156.6° W) are

289   from the ARM Climate Modeling Best Estimate product (Xie et al., 2010). The liquid water

290 path (LWP) and ice water path (IWP) data are obtained from Zhao et al. (2012).

291 Specifically, the Shupe and Turner's data are based on the retrievals of cloud properties

292 measured by the ARM Millimeter-Wavelength Cloud Radar (Shupe et al., 2005) and the

293 Microwave Radiometer (MWR) (Turner et al., 2007), with the uncertainties for liquid water

294 content (LWC) within 50% and for ice water content (IWC) within a factor of 2. For

295 Wang's data, IWP is retrieved from the combined ARM Millimeter-Wavelength Cloud

296 Radar and Micropulse lidar measurements (Wang and Sassen, 2002) with an uncertainty

297 of 35% (Khanal and Wang, 2015). LWP is retrieved from the ARM MWR measurements

298 with an uncertainty of 50% (Wang, 2007). For Deng's data, IWC is retrieved based on the

299 Millimeter-Wavelength Cloud Radar measurements with a retrieval error within 85%

300 (Deng and Mace, 2006). For Dong's data, LWC is retrieved from the MWR measurements

301 with an uncertainty within 113% (Dong and Mace, 2003). Note that measured IWC and

302 IWP cannot distinguish cloud ice from the snow. The simulated IWP and IWC therefore

303 include the snow component which is consistent with observations used in this study.

304   The ICNC was measured during the M-PACE single-layer mixed-phase stratus

305 period. The data includes 53 profiles measured in four flights over Barrow and Oliktok Point

306 (located at 70.5° N, 149.9° W) by the University of North Dakota Citation aircraft. By

307 combining measurements from different probes, McFarquhar et al. (2007) provided cloud

308 particle size distributions over a continuous size range. The forward scattering spectrometer

309 probe (FSSP) measured particle number concentrations with particle diameters between 3 to

310   53 μm, while the one-dimensional cloud probe (1DC) counted cloud particles ranging from

311   20 to 620 μm. The two-dimensional cloud probe (2DC) covered particle sizes from 30 to 960

312   μm, while the high-volume precipitation sampler (HVPS) sampled particles from 0.4 to 40

313   mm. The data were collected every 10 seconds but were averaged to 30 s^{-1} to ensure adequate

314   statistical sampling. The cloud phase was identified by detecting the presence of supercooled

315   droplets by the Rosemount Icing Detector (RICE). In mixed-phase clouds, any particles

316   larger than 125 μm are identified as ice particles, and cloud particles smaller than 53 μm are

317   counted as liquid-phase particles. Particles with a diameter ranging from 53 to 125 μm are

318   counted as a liquid when there is drizzle, and as ice, if there is no drizzle. A more detailed

319   description of the particle phase identification algorithm can be found in McFarquhar et al.

320   (2007). When comparing the simulated ICNC with the observations, we only consider ice

321   particles larger than 53 μm, as the observations were limited to ice particles larger than 53

322   μm.

323   However, the M-PACE data were collected before the advent of shatter mitigating

324   tips and before algorithms for removing the shattered particles had been developed. Thus,

325   there are no corrections for the shattering effect in these data. Previous studies indicated an

326   averaged reduction of ice number concentrations by 1-4.5 times and up to a factor of 10

327   (for some data samples) in other field campaigns, such as the Instrumentation Development

328   and Education in Airborne Science 2011 (IDEAS-2011), the Holographic Detector for

329   Clouds (HOLODEC), and the Indirect and Semidirect Aerosol Campaign (ISDAC), which

330   also used the 2DC cloud probe, but adopted anti-shattering tips and algorithms for

331   removing the shattered particles (Jackson and McFarquhar, 2014; Jackson et al., 2014). In

332   order to account for the anti-shattering effect, observed ice number concentrations were

333   scaled by a factor of 1/4 and 1/2, respectively, to consider the possible range of the

334   shattering effect. Furthermore, to be consistent with Figure 10 in Jackson et al. (2014), only

335   ice particles with diameters larger than 100 μm are included in our model and observation

336   intercomparisons.

337   **3.3 Model set up and description of model experiments**

338   In this study, we run SCAM with 32 vertical layers from the surface up to 3 hPa. The

339   model is initialized and driven by the large-scale forcing data at every 3 hours. The forcing

340   data developed by Xie et al. (2006) include the divergences and advections of moisture and

341   temperature as well as the surface flux. The simulation period is from 5 to 22 October 2004

342   and covers the second and third synoptic regimes and the transition period between them.

343   A detailed description of model experiments along with SIP mechanisms in these

344   experiments is provided in Table 1. The control experiment (CTL) uses the default CAM6

345   model that only includes the SIP due to the HM process. The impacts of two new SIP

346   mechanisms, including the ice-ice collision break-up and rain freezing fragmentation based

347   on Phillips et al. (2017a, 2018) are addressed in the SIP_PHIL experiment. To examine the

348   impact of rime splintering in the CTL experiment, we conducted CTL_no_HM experiment

349   that is similar to CTL but without the HM process.

350

351   4 Results

352   4.1 SIP impacts on different types of clouds during M-PACE

353   Figure 4 shows the temporal evolution of LWP, IWP, and cloud fractions from two

354   model simulations (CTL and SIP_PHIL) and their comparison to observations. The model

355   simulations cover the second and third synoptic regimes as well as the transition period

356   between them. Two different types of clouds were formed in response to the strong surface

357   forcing during the second synoptic regime from 4 to 14 October. As shown in Fig. 4c,

358   multilayer stratus occurred from 5 to 8 October, and the clouds extended from 950 hPa up to

359   500 hPa. Between 9 and 14 October, single-layer boundary layer stratus occurred between

360   800 and 950 hPa. Because of the dramatic change in cloud types in the second regime, we

361   further separate the second regime into two time periods. Then, we select typical days in the

362   four time periods for our analysis in this study, as shown in Fig. 4. The period from 6 to 8

363   October is selected as the "multilayer stratus" period. The period from 9 to 12 October is

364   selected as the "single-layer stratus" period, followed by the transition period marked on 16

365   October. The period between 18 and 20 October is selected to represent the "frontal cloud"

366   type during the third regime.

367   Figure 4 shows that the simulated IWP is systematically underestimated during M-

368   PACE in the CTL experiment. The maximum value of IWP in CTL is smaller than 50 g m$^-$

369   ^{2} during M-PACE, but up to 500 g m^{-2} in the measurements. The SIP_PHIL experiment

370   shows decreased LWP and increased IWP compared with CTL, reaching a better agreement

371   with the measurements. For example, IWP increases from 50 g m^{-2} in CTL to 425 g m^{-2} in

372   SIP_PHIL on 20 October, compared with $300 \sim 475$ g m^{-2} from different measurements (Fig.

373   4). The simulated LWP is overestimated during the "multilayer stratus", the second half of

374   the "single-stratus", and the "frontal cloud" periods in CTL, particularly on 20 October.

375   The SIP_PHIL experiment decreases the LWP from 550 g m^{-2} in CTL to 300 g m^{-2} on 11

376   October and from 425 g m^{-2} in CTL to 70 g m^{-2} on 20 October (Fig. 4a). The CTL_no_HM

377   experiment has similar results as the CTL experiment.

378   During the multilayer stratus period, the CTL and SIP_PHIL experiments show that the

379   cloud top is located at about 5 km with a temperature of –20 °C (Fig. 5). These cloud

380   properties are consistent with the observations (Verlinde et al., 2007) that show a minimum

381   observed cloud temperature of –17°C (Fig. 4). However, we notice a significant

382   overestimation of cloud amount at 6–8 km on 7 October by the model simulations in Fig. 5,

383   as compared to the observation in Fig. 4c.

384   During this period, IWC is increased in the SIP_PHIL experiment compared to CTL,

385   while LWC is decreased. The mean vertical profiles of simulated IWC and LWC in this

386   period are shown in Fig. 6. The simulated values of LWC and IWC are lower than

387   observations, particularly for IWC. LWC decreases from 130 mg m^{-3} in CTL to 80 mg m^{-3}

388   in SIP_PHIL below 1 km. IWC increases from 3 mg m^{-3} in CTL to 5 mg m^{-3} in SIP_PHIL.

389   The time-averaged IWP increases from 11.2 g m^{-2} in CTL to 17.1 g m^{-2} in SIP_PHIL but is

390   still lower than the observed value of 55.6 g m^{-2} (Table 2). After considering the SIP in the

391   model, for the multilayer stratus period, ICNC is increased by 1 L^{-1} (Fig. 5) at an altitude of

392   1 to 4 km. Observations of ICNC are not available during this period.

393   Between 9 and 14 October, a persistent boundary-layer mixed-phase stratus occurred

394   between 800-950 hPa, with the cloud top temperature at around $-15\,°C$ (Verlinde et al., 2007).

395   This single-layer stratus was separated from the surface based on the measurement (Fig. 4c).

396   However, modeled clouds extend to the surface in CTL (Fig. 5). This bias is alleviated in

397   SIP_PHIL on 8 and 11 October (Fig. 5). Previous studies also found that this bias partially

398   results from the overestimation of low-level moisture in the large-scale forcing data (Zhang

399   et al., 2019, 2020).

400   Observed cloud liquid is located above the cloud ice during this period, with the LWC

401   peak ~0.5 km above the IWC peak. Observed vertical profile of LWC shows a maximum of

402   300 mg m^{-3} (ranging from 210 to 500 mg m^{-3}) at ~1.25 km, while observed IWC is peaked

403   at 0.75 km (Fig. 6). This characteristic is clearly captured by the SIP_PHIL experiment, with

404 the peaks of LWC and IWC located at 0.75 and 0.5 km, respectively (Fig. 6). A better relative

405 position of cloud liquid and ice in SIP_PHIL indicates a better simulation of interactions

406 between cloud physics and dynamics. This distinct feature also contributes to the longevity

407 of mixed-phase clouds in the Arctic, as discussed in Section 1. In SIP_PHIL, the maximum

408 IWC value is four times larger than that in CTL (2 versus 0.5 mg m^{-3}); accordingly,

409 temporally-averaged IWP increases from 0.9 in CTL to 2.5 g m^{-2} in SIP_PHIL (Table 2).

410 Meanwhile, ICNC in SIP_PHIL is higher than that in CTL, and the maximum ICNC goes

411 up by 5 L^{-1} at 0.5 km on 11 October (Fig. 5). Thus, SIP adds an extra source of ice crystals

412 to the boundary-layer mixed-phase stratus clouds.

413   During the transition period, several distinct liquid layers are interrupted by the ice

414 enriched layers in the observation. Due to the coarse vertical resolution, the model may not

415 be able to capture this vertical variation accurately. Considerable variation was noticed in the

416 observed IWC with a maximum IWC of 0.8–1.8 mg m^{-3} (Fig. 7). The CTL experiment

417 substantially underestimates IWC, as it produces IWC less than 0.1 mg m^{-3}. The maximum

418 IWC in SIP_PHIL is 1.15 mg m^{-3}, providing a better agreement with the observation. The

419 simulated peak LWC is decreased from 80 in CTL to 65 mg m^{-3} in SIP_PHIL, which is

420 closer to the observed value of 55 mg m^{-3}. The temporally-averaged IWP in SIP_PHIL is

421 10^4 times larger than that in CTL, with values of 0.0001, 3.6, and 5.6 g m^{-2} in CTL, SIP_PHIL,

422 and observation, respectively (Table 2). The vertically-integrated ICNC is 7.66 and 4.57×10^5

423 L^{-1} in CTL and SIP_PHIL, respectively (Table 2). Considering SIP in the model increases

424 vertically-integrated ICNC by five orders of magnitude during the transition period.

425 During the frontal cloud period, stratocumulus and altostratus clouds associated with

426 the frontal system extended from the surface up to 8 km (Fig. 4). The SIP_PHIL experiment

427 shows the largest absolute increases in IWC and ICNC compared to the other periods (Fig.

428 5). The peak of modeled IWC is located at 2.5 km, with values of 2 and 8 mg m^{-3} in CTL

429 and SIP_PHIL, respectively (Fig. 7), much lower than the observation (ranging from 8 to 40

430 mg m^{-3}). IWP is 10.4, 26.1, and 96 g m^{-2} in CTL, SIP_PHIL, and the observation,

431 respectively (Table 2). ICNC is increased by up to 7 L^{-1} between 2 to 4 km on 20 October

432 from CTL to SIP_PHIL (Fig. 5). The simulated LWP is decreased from 127.6 to 41.2 g m^{-2},

433 which is closer to the observed value of 50.2 g m^{-2}.

434 The relative importance of primary and secondary ice production is shown as pie

435 charts in Fig. 8, to identify the dominant ice production mechanism in different types of

436 the Arctic clouds. The primary ice production (i.e., ice nucleation) is more important in the

437 clouds with colder cloud tops, such as multilayer stratus and frontal clouds with cloud top

438 temperatures colder than –25 °C and –40 °C, respectively. The primary ice production

439 contributes 37% and 69% to the total ice production during the multilayer stratus and

440 frontal cloud periods, respectively. Primary ice production is more efficient in deep clouds

441 due to the inverse relationship between the ice nucleation rate and temperature. SIP is more

442 important than primary ice production in the boundary-layer stratus and in clouds during

443   the transition period when cloud top temperatures were at -15 °C. The fragmentation of

444   freezing raindrops contributes the most (up to 80%) to the ice production in the single-layer

445   boundary-layer stratus. The break-up from ice-ice collisions contributes 22% to the total

446   ice production in the frontal clouds, while the rime splintering contributes 22% to the

447   multilayer stratus. These two SIP mechanisms (i.e., break-up from ice-ice collisions and

448   rime splintering) account for a small fraction of the ice production in the boundary-layer

449   stratus.

450   Next, we will focus on the SIP impacts on the boundary-layer stratus related to the

451   phase partitioning (section 4.2) and ICNC (section 4.3).

452   4.2 SIP impact on occurrence and phase partitioning of the mixed-phase

453   clouds

454   Figure 9 shows the liquid fraction (defined as LWC/(LWC+IWC)) as a function of

455   normalized height in the single-layer boundary-layer stratus. The normalized height Z_n is 0

456   at cloud base and 1 at cloud top. IWC from the model includes all the ice hydrometeors to

457   compare it with observations. Fig. 9a reveals two features of the observed single-layer

458   boundary-layer clouds: (1) mixed-phase is dominant in the clouds, and (2) the liquid fraction

459   increases with cloud altitude. The liquid fraction is between 0.05 and 0.95 in most portions

460   of the clouds, indicating a mixed-phase feature in the observation. In the upper portion of the

461   clouds, observed liquid fraction is larger than 0.6 with the mean value increasing with height.

462   In the lower portion of the clouds ice mass fraction increases as a result of ice growth by

463   riming of cloud liquid and ice sedimentation from the upper levels. The CTL experiment

464   cannot reproduce the observed mixed-phase feature. A large portion of the clouds is in liquid

465   phase with the liquid fraction close to 1 in CTL, which significantly overestimates the liquid

466   fraction in the clouds. This is vastly different from previous versions of CAM. CAM5

467   showed an underestimation of the liquid fraction (Liu et al., 2011; Cesana et al., 2015; Tan

468   and Storelvmo, 2016; Zhang et al., 2019; Tan and Storelvmo, 2019), while CAM3 showed

469   a decrease of the liquid fraction with height due to its use of a temperature-dependent phase

470   partitioning (Liu et al., 2007).

471   The SIP_PHIL experiment improves the model simulation of cloud phase with

472   increased ice fraction in the bottom half of the clouds by adding an extra source of ice crystals

473   from SIP (Fig. 9c). The CTL_no_HM experiment gives very similar results as the CTL

474   experiment (Fig. 9d). Note that the modeled liquid fraction distributes on discrete vertical

475   levels (Fig. 9b, c, d) due to the coarse model vertical resolution (with only 10 vertical levels

476   below 2 km). In contrast, observed data were detected at $10 \ s^{-1}$ resolution during spiral

477   ascents and descents in the clouds so that the observed liquid fraction is distributed

478   continuously with height.

479   For the cloud occurrence, 62.7% of observed clouds are mixed-phase, and only 16%

480   are liquid-phase during the single-layer stratus period, as shown in Table 3. The liquid phase

481   cloud occurrence is 73% in CTL and only 26.9% for mixed-phase clouds, indicating too

482   much liquid-phase and too less mixed-phase occurrence in CAM6. The mixed-phase cloud

483   occurrence is 58.8% in SIP_PHIL and agrees much better with the observation. Thus, there

484   are more frequent mixed-phase clouds in SIP_PHIL. However, the occurrence of ice phase

485   is still underestimated and that of the liquid phase overestimated in SIP_PHIL. Note that, we

486   define the modeled clouds with total cloud water amount larger than 0.001 g m^{-3} and the

487   liquid fraction between 0.5% and 99.5% as the mixed-phase clouds, which are consistent

488   with the observation (McFarquhar et al., 2007).

489   4.3   SIP impact on ice crystal number concentration

490   4.3.1   Vertical distribution of ice crystal number concentration

491   The vertical distribution of ICNCs in the single-layer boundary-layer stratus clouds

492   on October 9, 10, and 11 from model simulations and observations is shown in Figure 10.

493   The measured ICNCs when applied with a correction factor of ¼ range from 0.02 to 20 L^{-}

494   ^{1}, with an average value of 1 L^{-1}. The CTL and CTL_no_HM experiments have similar

495   results, and both underestimate the ICNCs in all the cloud layers, with a mean ICNC of

496   ~0.1 L^{-1} and the maximum concentration of 1 L^{-1}. The mean ICNC is increased to ~1 L^{-1}

497   in the SIP_PHIL experiment with the maximum concentration of 30 L^{-1}, which are in better

498   agreement with the observations compared to CTL. ICNCs are increased by more than one

499   order of magnitude in the lower portion of the clouds, although they are still lower than

500   those observed in the upper portion of the clouds.

501   Figure 10 also shows the linear regressions of ICNCs as a function of cloud altitude

502   (black lines). ICNCs increase towards the cloud base in the observation, revealing ice

503   multiplication during the ice growth and sedimentation. The CTL experiment shows that

504   the ICNCs decrease towards the cloud base, an opposite pattern compared to the

505   observation. SIP_PHIL captures the observed pattern in the vertical profile of ICNCs (Fig.

506   10c), suggesting that SIP is an important source of ice crystals near the cloud base in the

507   Arctic boundary-layer mixed-phase stratus. Furthermore, the vertical distribution of ice

508   particles is important for the longevity of the Arctic mixed-phase clouds, which features

509   lower ICNCs in the upper portion of clouds and higher ICNCs towards the cloud base.

510   **4.3.2   PDF of ice crystal number concentration**

511   Figure 11 shows the probability density function (PDF) (i.e., the frequency of

512   occurrence) of ICNCs from model simulations and observations for the boundary-layer

513   mixed-phase stratus period (October 9-12, 2004). Note that only particles with a diameter

514   greater than 100 μm are included in the observed and modeled ICNCs. The PDF

515   distribution in SIP_PHIL shows a shift to the right, with the ICNC peak much closer to the

516   observations than CTL. The median ICNC is 0.13 L^{-1} in CTL, shifting to 0.27 L^{-1} in

517   SIP_PHIL, which is closer to the observed median value of 0.32 L^{-1}.

518   The PDF distribution in SIP_PHIL also has a broader distribution than CTL. A

519   broader distribution indicates that the maximum concentrations are higher in the

520   observation and SIP_PHIL compared to CTL. In the CTL experiment, the frequency of

521   occurrence of ICNCs is much lower (higher) than observations when their values are higher

522   (lower) than 0.1 L^{-1}. These biases in ICNCs PDF are much improved in SIP_PHIL, leading

523   to a better agreement with the observation. The frequency occurrence of ICNC at 1 L^{-1} is

524   2.12%, 10.37%, 13.77% in CTL, SIP_PHIL, and observation, respectively. Thus,

525   SIP_PHIL has an occurrence frequency of ICNC larger than 1 L^{-1}, which is 5 times of that

526   in CTL. We note that the agreement between modeled and observed ICNCs is improved

527   with a correction factor of ¼ (Figures 10 and 11) and a correction factor of ½

528   (supplementary Figures S2 and S4) to the observed ICNCs, compared to that without a

529   correction factor (Supplementary Figures S1 and S3). This is because model simulations

530   including SIP_PHIL underestimate the observed ICNCs without the correction of the

531   shattering effect.

532   **4.3.3   Dependence of ice enhancement on cloud temperature**

533   The bivariate joint PDF defined in terms of temperature and ice enhancement

534   (N_{SIP_PHIL}/N_{CTL}) during the M-PACE is shown in Fig. S5. Strong ice enhancements are

535   noticed at temperatures from –3 to –16°C, and ICNCs are increased by nearly 4 orders of

536   magnitude in SIP_PHIL compared with CTL. As temperature decreases below –35°C, ice

537 enhancement happens again, but with a reduced magnitude. For example, the largest

538 enhancement at –44°C is around 3.2, with a frequency of 1% to 7%.

539   To investigate the dominant processes that contribute to the strong enhancement

540 near –10 °C we plotted the bivariate joint PDF defined in terms of temperature and ice

541 production rate (Fig. 12). A clear relationship between ice enhancement and fragmentation

542 of freezing raindrops can be seen at temperatures from –20 to –4 °C in Fig. 12 and Fig. S5.

543 The maximum ice production from the fragmentation of freezing raindrops is 160 L^{-1} (i.e.,

544 10$^{2.2}$) at temperatures ranging from –8 to –14 °C. Even though rime splintering also

545 happens at temperatures between –8 to –3 °C with a maximum value of 20 L^{-1}, its ice

546 production is almost one order of magnitude lower than that from the fragmentation of

547 freezing raindrops. Between –20 to –16 °C, primary ice nucleation and fragmentation of

548 freezing raindrops coexist, with the fragmentation of freezing raindrops more efficient

549 (with a magnitude of 10 L^{-1}) comparing to the primary ice nucleation (about 1 L^{-1}). Primary

550 ice nucleation has the largest production of up to 250 L^{-1} at temperatures ranging from –

551 32 to –25 °C. Below –35 °C, ice-ice collision break-up frequently happens, but with a lower

552 process rate.

553   In summary, the strongest ice enhancement occurs in the moderately supercooled

554 clouds with temperatures around –10°C. ICNCs are increased by up to 4 orders of

555 magnitude mainly from the fragmentation of freezing raindrops. A weaker ice

556 enhancement is noticed frequently in ice clouds with temperatures below –35°C, which is

557 attributed to the ice-ice collision break-up.

5   Summary, conclusions and outlook

559 In this study, two new SIP mechanisms are implemented in a GCM model (CAM6)

560 to investigate their impacts on the Arctic mixed-phase clouds, which were observed during

561 the DOE ARM M-PACE field campaign. The CAM6 model with the new SIP provides a

562 better simulation of the distinct "liquid cloud top, ice cloud base" feature of long-lived

563 Arctic boundary-layer mixed-phase clouds.

564 We find that model biases of underestimation of mixed-phase cloud occurrence and

565 overestimation of pure liquid cloud occurrence are reduced for the single-layer stratus after

566 considering the new SIP processes. The mixed-phase cloud occurrence is 26.9%, 58.8%, and

567 62.7% in CTL, SIP_PHIL and the observation, respectively, while the pure liquid cloud

568 occurrence is reduced from 73% in CTL to 40% in SIP_PHIL, in a better agreement with

569 observed 16%.

570 We find that the pattern of the vertical distribution of ICNCs in the single-layer

571 stratus is reversed after considering the new SIP processes in the model. The measured

572 decrease of ICNCs with cloud height is captured by SIP_PHIL but not by CTL. SIP also

573 leads to a shift of PDF of ICNCs towards a more frequent occurrence of high ICNCs and

574 a less frequent occurrence of low ICNCs. We notice a taller PDF with higher peak and a

575 broader tail in SIP_PHIL, indicating that high ICNCs occur more frequently with the

576 occurrence of extreme high ICNCs ($>10^2$ L^{-1}) in SIP_PHIL, which is absent in CTL.

577   The maximum ICNC is around 1, 30, and 20 L^{-1} in CTL, SIP_PHIL, and

578 observation, respectively, in the single-layer stratus. During the frontal cloud period, the

579 SIP_PHIL experiment shows the largest absolute increases in IWC and ICNC by 6 mg m^{-3}

580 and 7 L^{-1}, respectively. The largest ice enhancement (N_{SIP_PHIL}/N_{CTL}) is noticed during the

581 transition period with a moderately cold cloud top temperature. The column integrated ICNC

582 increases by five orders of magnitude and IWP increases by four orders of magnitude in

583 SIP_PHIL compared to CTL. When comparing the relative importance between primary

584 and secondary ice production, we notice that primary ice nucleation is more dominant in

585 the deep clouds with cloud tops reaching up to 10 km. At the same time, the fragmentation

586 of freezing raindrops contributes more to ICNCs in the boundary-layer clouds.

587   At temperatures from –4 to –20 °C, significant ice enhancement is attributed to the

588 fragmentation of freezing raindrops, with the maximum ice production of 160 L^{-1} at –10 °C.

589 A weaker ice enhancement due to ice-ice collision break-up is noticed in ice clouds with

590 temperatures below –35 °C but with unneglectable occurrence frequencies. Primary ice

591 nucleation has the largest production by up to 251 L^{-1} in the relatively cold-mixed phase

592 clouds with temperatures between –32 to –25 °C.

593   In summary, the consideration of the new SIP processes in CAM6 results in a

594   significant improvement in the model simulated clouds during M-PACE. It underscores

595   the critical role of SIP in cloud microphysics, which should be considered in the

596   parameterizations of GCMs.

597   In this study, the parameterization of the HM process rate is based on Cotton et al.

598   (1986). In this parameterization the ice production rate does not have a dependence on

599   droplet size. Lacking the effect of cloud droplet spectrum in the HM process is supposed to

600   result in an overestimated splintering rate in the Arctic clouds, especially for the clouds with

601   cloud-bases close to the freezing level and with small droplets in the clouds. However, the

602   overestimation in the HM splintering rate due to lack of the cloud droplet spectrum might be

603   balanced by neglecting the raindrop splintering in the HM process in the MG microphysics.

604   In this study, we keep using the bulk approach to represent the HM process, to be the same

605   as that in the standard MG microphysics scheme. It would be interesting to examine the

606   impact of a bin approach to represent the HM process on modeled clouds, which will be a

607   topic of our future studies.

608   For the ice fragmentation from ice-ice collisions, the graupel related collisions are

609   not included in this study, because the current MG microphysical scheme does not treat

610   graupel. To quantify the impacts of graupel on SIP, the cloud microphysical scheme with

611   prognostic graupel (Gettelman et al., 2019) or a "Single-Ice" microphysical scheme

612   (Morrison and Milbrandt, 2015; Zhao et al., 2017) will be needed.

613   We note that the representation of ice properties is highly simplified in the current

614   model. Firstly, ice particles in nature are featured with continuous size distributions with

615   complex shapes and a wide range of densities. In contrast, the current model artificially

616   classifies them into two categories (i.e., cloud ice and snow) with fixed densities, e.g.,

617   densities of 500 kg m^{-3} for cloud ice and of 250 kg m^{-3} for snow. Moreover, the shape of

618   all ice particles is assumed to be spherical. The parameters, a and b in the relationship of

619   terminal velocity and diameter (V-D, $V=aD^b$) are fixed values for cloud ice and snow.

620   These assumptions cannot represent the complexities of ice properties (e.g., size

621   distribution, density, shape, and fall speed) in the measurement. Lastly, the riming intensity

622   of ice particles changes as ice collides with supercooled liquid, leading to significant

623   changes in density and fall speed of ice. This evolution of ice properties is currently not

624   represented in the model. A promising method is to represent the ice-phase microphysics

625   with varying ice properties (Morrison and Milbrandt, 2015; Zhao et al., 2017).

626

627   **Competing interests:** The authors declare that they have no conflict of interest.

628

629   **Data availability:** The code for the Community Earth System Model version 2 (CESM) is

630   freely available at http://www.cesm.ucar.edu/models/cesm2 (last access: 3 March 2021,

631   Danabasoglu et al., 2020). The model datasets and secondary ice production code are

632   archived at the NCAR Cheyenne supercomputer and are available upon request. The

633 observation data of M-PACE campaign is obtained from the Atmospheric Radiation

634 Measurement (ARM) user facility, a U.S. Department of Energy Office of Science,

635 available at https://www.arm.gov/research/campaigns/nsa2004arcticcld (last access: 3

636 March 2021; McFarquhar et al., 2007; Verlinde et al., 2007).

637

638 **Author contributions**: XZ and XL conceptualized the analysis and wrote the manuscript

639 with input from the co-authors. XZ modified the code, carried out the simulations, and

640 performed the analysis. VP and SP provided the model code for the secondary ice

641 production. VP and SP also provided scientific suggestions to the manuscript. XL was

642 involved with obtaining the project grant and supervised the study. All authors were

643 involved in helpful discussions and contributed to the manuscript.

644

645 **Acknowledgment:** This research was supported by the DOE Atmospheric System

646 Research (ASR) Program (grant DE-SC0020510). We thank Meng Zhang for helpful

647 discussions especially on processing the observation data. We thank Dr. Chuanfeng Zhao

648 and Dr. Greg McFarquhar for their suggestions on processing the observation data.

649

Reference

Bennartz, R., Shupe, M. D., Turner, D. D., Walden, V. P., Steffen, K., Cox, C. J., Kulie, M. S., Miller, N. B., and Pettersen, C.: July 2012 Greenland melt extent enhanced by low-level liquid clouds, Nature, 496, 83-86, 10.1038/nature12002, 2013.

Cesana, G., and Chepfer, H.: Evaluation of the cloud thermodynamic phase in a climate model using CALIPSO-GOCCP, Journal of Geophysical Research Atmospheres, 118, 7922-7937, 10.1002/jgrd.50376, 2013.

Cesana, G., Waliser, D. E., Jiang, X., and Li, J. L. F.: Multimodel evaluation of cloud phase transition using satellite and reanalysis data, Journal of Geophysical Research: Atmospheres, 120, 7871-7892, 10.1002/2014JD022932, 2015.

Connolly, P. J., Heymsfield, A. J., and Choularton, T. W.: Modelling the influence of rimer surface temperature on the glaciation of intense thunderstorms: The rime–splinter mechanism of ice multiplication, Q J Roy Meteor Soc, 132, 3059-3077, 10.1256/qj.05.45, 2006.

Cotton, W. R., Tripoli, G. J., Rauber, R. M., and Mulvihill, E. A.: Numerical Simulation of the Effects of Varying Ice Crystal Nucleation Rates and Aggregation Processes on Orographic Snowfall, American Meteorological Society, 1658-1680, 1986.

Danabasoglu, G., Lamarque, J. F., Bacmeister, J., Bailey, D. A., DuVivier, A. K., Edwards, J., Emmons, L. K., Fasullo, J., Garcia, R., Gettelman, A., Hannay, C., Holland, M. M., Large, W. G., Lauritzen, P. H., Lawrence, D. M., Lenaerts, J. T. M., Lindsay, K., Lipscomb, W. H., Mills, M. J., Neale, R., Oleson, K. W., Otto-Bliesner, B., Phillips, A. S., Sacks, W., Tilmes, S., van Kampenhout, L., Vertenstein, M., Bertini, A., Dennis, J., Deser, C., Fischer, C., Fox-Kemper, B., Kay, J. E., Kinnison, D., Kushner, P. J., Larson, V. E., Long, M. C., Mickelson, S., Moore, J. K., Nienhouse, E., Polvani, L., Rasch, P. J. and Strand, W. G.: The Community Earth System Model Version 2 (CESM2), Journal of Advances in Modeling Earth Systems, 12(2), https://doi.org/10.1029/2019MS001916, 2020.

Dearden, C., Vaughan, G., Tsai, T., and Chen, J. P.: Exploring the diabatic role of ice microphysical processes in two north atlantic summer cyclones, Mon Weather Rev, 144, 1249-1272, 10.1175/MWR-D-15-0253.1, 2016.

Deng, M., and Mace, G. G.: Cirrus microphysical properties and air motion statistics using cloud radar Doppler moments. Part I: Algorithm description, J Appl Meteorol Clim, 45, 1690-1709, 10.1175/JAM2433.1, 2006.

Dong, X., and Mace, G. G.: Profiles of low-level stratus cloud microphysics deduced from ground-based measurements, J Atmos Ocean Tech, 20, 42-53, 10.1175/1520-0426(2003)020<0042:POLLSC>2.0.CO;2, 2003.

686 Feingold, G., Walko, R. L., Stevens, B., and Cotton, W. R.: Simulations of marine
687   stratocumulus using a new microphysical parameterization scheme, Atmospheric
688   Research, 47-48, 505-528, 10.1016/S0169-8095(98)00058-1, 1998.
689 Field, P. R., Lawson, R. P., Brown, P. R. A., Lloyd, G., Westbrook, C., Moisseev, D.,
690   Miltenberger, A., Nenes, A., Blyth, A., Choularton, T., Connolly, P., Buehl, J.,
691   Crosier, J., Cui, Z., Dearden, C., DeMott, P., Flossmann, A., Heymsfield, A., Huang,
692   Y., Kalesse, H., Kanji, Z. A., Korolev, A., Kirchgaessner, A., Lasher-Trapp, S.,
693   Leisner, T., McFarquhar, G., Phillips, V., Stith, J., and Sullivan, S.: Chapter 7.
694   Secondary Ice Production - current state of the science and recommendations for the
695   future, Meteorological Monographs, 58, 7.1-7.20, 10.1175/amsmonographs-d-16-
696   0014.1, 2016.
697 Fu, S., Deng, X., Shupe, M. D., and Xue, H.: A modelling study of the continuous ice
698   formation in an autumnal Arctic mixed-phase cloud case, Atmospheric Research,
699   228, 77-85, 10.1016/j.atmosres.2019.05.021, 2019.
700 Gettelman, A. and Morrison, H.: Advanced two-moment bulk microphysics for global
701   models. Part I: Off-line tests and comparison with other schemes, Journal of
702   Climate, 28(3), 1268–1287, https://doi.org/10.1175/JCLI-D-14-00102.1, 2015.
703 Gettelman, A., Morrison, H., Thayer-Calder, K., and Zarzycki, C. M.: The Impact of
704   Rimed Ice Hydrometeors on Global and Regional Climate, Journal of Advances in
705   Modeling Earth Systems, 11, 1543-1562, 10.1029/2018MS001488, 2019.
706 Golaz, J. C., Larson, V. E., and Cotton, W. R.: A PDF-based model for boundary layer
707   clouds. Part I: Method and model description, Journal of the Atmospheric Sciences,
708   59, 3540-3551, 10.1175/1520-0469(2002)059<3540:APBMFB>2.0.CO;2, 2002.
709 Grabowski, W. W., Thouron, O., Pinty, J. P., and Brenguier, J. L.: A hybrid bulk-bin
710   approach to model warm-rain processes, Journal of the Atmospheric Sciences, 67,
711   385-399, 10.1175/2009JAS3155.1, 2010.
712 Intrieri, J. M., Shupe, M. D., Uttal, T., and McCarty, B. J.: An annual cycle of Arctic
713   cloud characteristics observed by radar and lidar at SHEBA, Journal of Geophysical
714   Research: Oceans, 107, SHE 5-1, 10.1029/2000jc000423, 2002.
715 Jackson, R. C., and McFarquhar, G. M.: An assessment of the impact of antishattering
716   tips and artifact removal techniques on bulk cloud ice microphysical and optical
717   properties measured by the 2D cloud probe, J Atmos Ocean Tech, 31, 2131-2144,
718   10.1175/JTECH-D-14-00018.1, 2014.
719 Jackson, R. C., McFarquhar, G. M., Stith, J., Beals, M., Shaw, R. A., Jensen, J., Fugal, J.,
720   and Korolev, A.: An assessment of the impact of antishattering tips and artifact
721   removal techniques on cloud ice size distributions measured by the 2D cloud probe,
722   J Atmos Ocean Tech, 31, 2567-2590, 10.1175/JTECH-D-13-00239.1, 2014.
723 Jiang, H., Cotton, W. R., Pinto, J. O., Curry, J. A. and Weissbluth, M. J.: Cloud resolving
724   simulations of mixed-phase Arctic stratus observed during BASE: Sensitivity to

725   concentration of ice crystals and large-scale heat and moisture advection, Journal of
726   the Atmospheric Sciences, 57(13), 2105–2117, https://doi.org/10.1175/1520-
727   0469(2000)057<2105:CRSOMP>2.0.CO;2, 2000.

728 Kay, J. E. and Gettelman, A.: Cloud influence on and response to seasonal Arctic sea ice
729   loss, Journal of Geophysical Research, 114(D18), D18204,
730   https://doi.org/10.1029/2009JD011773, 2009.

731 Khanal, S., and Wang, Z.: Evaluation of the lidar-radar cloud ice water content retrievals
732   using collocated in situ measurements, J Appl Meteorol Clim, 54, 2087-2097,
733   10.1175/JAMC-D-15-0040.1, 2015.

734 Korolev, A. and Field, P. R.: The effect of dynamics on mixed-phase clouds: Theoretical
735   considerations, Journal of the Atmospheric Sciences, 65(1), 66–86,
736   https://doi.org/10.1175/2007JAS2355.1, 2008.

737 Kuba, N., and Murakami, M.: Effect of hygroscopic seeding on warm rain clouds –
738   numerical study using a hybrid cloud microphysical model, Atmos Chem Phys, 10,
739   3335-3351, 10.5194/acp-10-3335-2010, 2010.

740 Larson, V. E., Golaz, J.-C., and Cotton, W. R.: Small-Scale and Mesoscale Variability in
741   Cloudy Boundary Layers: Joint Probability Density Functions, Journal of the
742   Atmospheric Sciences, 59, 3519-3539, 10.1175/1520-
743   0469(2002)059<3519:SSAMVI>2.0.CO;2, 2002.

744 Liu, X., Easter, R. C., Ghan, S. J., Zaveri, R., Rasch, P., Shi, X., Lamarque, J. F.,
745   Gettelman, A., Morrison, H., Vitt, F., Conley, A., Park, S., Neale, R., Hannay, C.,
746   Ekman, A. M. L., Hess, P., Mahowald, N., Collins, W., Iacono, M. J., Bretherton, C.
747   S., Flanner, M. G., and Mitchell, D.: Toward a minimal representation of aerosols in
748   climate models: description and evaluation in the Community Atmosphere Model
749   CAM5, Geosci Model Dev, 5, 709-739, 2012.

750 Liu, X., Ma, P. L., Wang, H., Tilmes, S., Singh, B., Easter, R. C., Ghan, S. J., and Rasch,
751   P. J.: Description and evaluation of a new four-mode version of the Modal Aerosol
752   Module (MAM4) within version 5.3 of the Community Atmosphere Model, Geosci
753   Model Dev, 9, 505-522, 2016.

754 Liu, X., and Penner, J. E.: Ice nucleation parameterization for global models,
755   Meteorologische Zeitschrift, 499-514, 10.1127/0941-2948/2005/0059, 2005.

756 Liu, X., Xie, S., Boyle, J., Klein, S. A., Shi, X., Wang, Z., Lin, W., Ghan, S. J., Earle, M.,
757   Liu, P. S. K. and Zelenyuk, A.: Testing cloud microphysics parameterizations in
758   NCAR CAM5 with ISDAC and M-PACE observations, Journal of Geophysical
759   Research, 116(24), D00T11, https://doi.org/10.1029/2011JD015889, 2011.

760 Liu, X., Xie, S. and Ghan, S. J.: Evaluation of a new mixed-phase cloud microphysics
761   parameterization with CAM3 single-column model and M-PACE observations,
762   Geophysical Research Letters, 34(23), L23712,
763   https://doi.org/10.1029/2007GL031446, 2007.

McFarquhar, G. M., Zhang, G., Poellot, M. R., Kok, G. L., McCoy, R., Tooman, T., Fridlind, A. and Heymsfield, A. J.: Ice properties of single-layer stratocumulus during the Mixed-Phase Arctic Cloud Experiment: 1. Observations, Journal of Geophysical Research, 112(D24), D24201, https://doi.org/10.1029/2007JD008633, 2007.

Morrison, H., de Boer, G., Feingold, G., Harrington, J., Shupe, M. D. and Sulia, K.: Resilience of persistent Arctic mixed-phase clouds, Nature Geoscience, 5(1), 11–17, https://doi.org/10.1038/ngeo1332, 2012.

Morrison, H., and Milbrandt, J. A.: Parameterization of cloud microphysics based on the prediction of bulk ice particle properties. Part I: Scheme description and idealized tests, Journal of the Atmospheric Sciences, 72, 287-311, 10.1175/JAS-D-14-0065.1, 2015.

Mossop, S. C.: The influence of drop size distribution on the production of secondary ice particles during graupel growth, Q J Roy Meteor Soc, 104, 323-330, 10.1002/qj.49710444007, 1978.

Onishi, R., and Takahashi, K.: A warm-bin-cold-bulk hybrid cloud microphysical model, Journal of the Atmospheric Sciences, 69, 1474-1497, 10.1175/JAS-D-11-0166.1, 2012.

Phillips, V. T. J., Blyth, A. M., Brown, P. R. A., Choularton, T. W., and Latham, J.: The glaciation of a cumulus cloud over New Mexico, Q J Roy Meteor Soc, 127, 1513-1534, 10.1002/qj.49712757503, 2001.

Phillips, V. T. J., Patade, S., Gutierrez, J., and Bansemer, A.: Secondary ice production by fragmentation of freezing drops: Formulation and theory, Journal of the Atmospheric Sciences, 75, 3031-3070, 10.1175/JAS-D-17-0190.1, 2018.

Phillips, V. T. J., Yano, J. I., Formenton, M., Ilotoviz, E., Kanawade, V., Kudzotsa, I., Sun, J., Bansemer, A., Detwiler, A. G., Khain, A., and Tessendorf, S. A.: Ice multiplication by breakup in ice-ice collisions. Part II: Numerical simulations, Journal of the Atmospheric Sciences, 74, 2789-2811, 10.1175/JAS-D-16-0223.1, 2017.

Phillips, V. T. J., Yano, J. I., and Khain, A.: Ice multiplication by breakup in ice-ice collisions. Part I: Theoretical formulation, Journal of the Atmospheric Sciences, 74, 1705-1719, 10.1175/JAS-D-16-0224.1, 2017.

Pinto, J. O.: Autumnal mixed-phase cloudy boundary layers in the arctic, Journal of the Atmospheric Sciences, 55(11), 2016–2038, https://doi.org/10.1175/1520-0469(1998)055<2016:AMPCBL>2.0.CO;2, 1998.

Schwarzenboeck, A., Shcherbakov, V., Lefevre, R., Gayet, J. F., Pointin, Y., and Duroure, C.: Indications for stellar-crystal fragmentation in Arctic clouds, Atmospheric Research, 92, 220-228, 10.1016/j.atmosres.2008.10.002, 2009.

802 Shupe, M. D. and Intrieri, J. M.: Cloud radiative forcing of the Arctic surface: The
803   influence of cloud properties, surface albedo, and solar zenith angle, Journal of
804   Climate, 17(3), 616–628, https://doi.org/10.1175/1520-
805   0442(2004)017<0616:CRFOTA>2.0.CO;2, 2004.
806 Shupe, M. D., Matrosov, S. Y., and Uttal, T.: Arctic mixed-phase cloud properties
807   derived from surface-based sensors at SHEBA, Journal of the Atmospheric
808   Sciences, 63, 697-711, 10.1175/JAS3659.1, 2006.
809 Shupe, M. D., Uttal, T., and Matrosov, S. Y.: Arctic cloud microphysics retrievals from
810   surface-based remote sensors at SHEBA, J Appl Meteorol, 44, 1544-1562,
811   10.1175/JAM2297.1, 2005.
812 Sotiropoulou, G., Sullivan, S., Savre, J., Lloyd, G., Lachlan-Cope, T., Ekman, A. M. L.,
813   and Nenes, A.: The impact of secondary ice production on Arctic stratocumulus,
814   Atmos Chem Phys, 20, 1301-1316, 10.5194/acp-20-1301-2020, 2020.
815 Sotiropoulou, G., Vignon, E., Young, G., Morrison, H., O'Shea, S., Lachlan-Cope, T.,
816   Berne, A., and Nenes, A.: Secondary ice production in summer clouds over the
817   Antarctic coast: an underappreciated process in atmospheric models, Atmos Chem
818   Phys, 1-30, 10.5194/acp-2020-328, 2020.
819 Sullivan, S. C., Barthlott, C., Crosier, J., Zhukov, I., Nenes, A., and Hoose, C.: The effect
820   of secondary ice production parameterization on the simulation of a cold frontal
821   rainband, Atmos Chem Phys, 18, 16461-16480, 10.5194/acp-18-16461-2018, 2018.
822 Sullivan, S. C., Hoose, C., Kiselev, A., Leisner, T., and Nenes, A.: Initiation of secondary
823   ice production in clouds, Atmos Chem Phys, 18, 1593-1610, 10.5194/acp-18-1593-
824   2018, 2018.
825 Sullivan, S. C., Hoose, C., and Nenes, A.: Investigating the contribution of secondary ice
826   production to in-cloud ice crystal numbers, Journal of Geophysical Research:
827   Atmospheres, 122, 9391-9412, 10.1002/2017JD026546, 2017.
828 Tan, I., and Storelvmo, T.: Sensitivity study on the influence of cloud microphysical
829   parameters on mixed-phase cloud thermodynamic phase partitioning in CAM5,
830   Journal of the Atmospheric Sciences, 73, 709-728, 10.1175/JAS-D-15-0152.1, 2016.
831 Tan, I., and Storelvmo, T.: Evidence of Strong Contributions From Mixed-Phase Clouds
832   to Arctic Climate Change, Geophys Res Lett, 46, 2894-2902,
833   10.1029/2018GL081871, 2019.
834 Turner, D. D., Clough, S. A., Liljegren, J. C., Clothiaux, E. E., Cady-Pereira, K. E., and
835   Gaustad, K. L.: Retrieving liquid water path and precipitable water vapor from the
836   atmospheric radiation measurement (ARM) microwave radiometers, 3680-3689,
837   2007.
838 Vavrus, S.: The impact of cloud feedbacks on Arctic climate under Greenhouse forcing,
839   Journal of Climate, 17, 603-615, 10.1175/1520-
840   0442(2004)017<0603:TIOCFO>2.0.CO;2, 2004.

841   Verlinde, J., Harrington, J. Y., McFarquhar, G. M., Yannuzzi, V. T., Avramov, A.,
842   Greenberg, S., Johnson, N., Zhang, G., Poellot, M. R., Mather, J. H., Turner, D. D.,
843   Eloranta, E. W., Zak, B. D., Prenni, A. J., Daniel, J. S., Kok, G. L., Tobin, D. C.,
844   Holz, R., Sassen, K., Spangenberg, D., Minnis, P., Tooman, T. P., Ivey, M. D.,
845   Richardson, S. J., Bahrmann, C. P., Shupe, M., DeMott, P. J., Heymsfield, A. J., and
846   Schofield, R.: The mixed-phase arctic cloud experiment, B Am Meteorol Soc, 88,
847   205-221, 10.1175/BAMS-88-2-205, 2007.
848   Wang, Y., Liu, X., Hoose, C., and Wang, B.: Different contact angle distributions for
849   heterogeneous ice nucleation in the Community Atmospheric Model version 5,
850   Atmos Chem Phys, 14, 10411-10430, 2014.
851   Wang, Z.: A refined two-channel microwave radiometer liquid water path retrieval for
852   cold regions by using multiple-sensor measurements, Ieee Geosci Remote S, 4, 591-
853   595, 10.1109/LGRS.2007.900752, 2007.
854   Wang, Z., and Sassen, K.: Cirrus cloud microphysical property retrieval using lidar and
855   radar measurements. Part I: Algorithm description and comparison with in situ data,
856   J Appl Meteorol, 41, 218-229, 10.1175/1520-
857   0450(2002)041<0218:CCMPRU>2.0.CO;2, 2002.
858   Xie, S., Boyle, J., Klein, S. A., Liu, X., and Ghan, S.: Simulations of Arctic mixed-phase
859   clouds in forecasts with CAM3 and AM2 for M-PACE, Journal of Geophysical
860   Research, 113, D04211-D04211, 10.1029/2007JD009225, 2008.
861   Xie, S., Klein, S. A., Yio, J. J., Beljaars, A. C. M., Long, C. N., and Zhang, M.: An
862   assessment of ECMWF analyses and model forecasts over the North Slope of
863   Alaska using observations from the ARM Mixed-Phase Arctic Cloud Experiment,
864   Journal of Geophysical Research, 111, D05107-D05107, 10.1029/2005JD006509,
865   2006.
866   Xie, S., McCoy, R. B., Klein, S. A., Cederwall, R. T., Wiscombe, W. J., Clothiaux, E. E.,
867   Gaustad, K. L., Golaz, J. C., Hall, S. D., Jensen, M. P., Johnson, K. L., Lin, Y.,
868   Long, C. N., Mather, J. H., McCord, R. A., McFarlane, S. A., Palanisamy, G., Shi,
869   Y., and Turner, D. D.: ARM climate modeling best estimate data: A new data
870   product for climate studies, B Am Meteorol Soc, 91, 13-20,
871   10.1175/2009BAMS2891.1, 2010.
872   Zhang, M., Liu, X., Diao, M., D'Alessandro, J. J., Wang, Y., Wu, C., Zhang, D., Wang,
873   Z., and Xie, S.: Impacts of Representing Heterogeneous Distribution of Cloud
874   Liquid and Ice on Phase Partitioning of Arctic Mixed-Phase Clouds with NCAR
875   CAM5, Journal of Geophysical Research: Atmospheres, 124, 13071-13090,
876   10.1029/2019JD030502, 2019.
877   Zhang, M., Xie, S., Liu, X., Lin, W., Zhang, K., Ma, H. Y., Zheng, X., and Zhang, Y.:
878   Toward Understanding the Simulated Phase Partitioning of Arctic Single-Layer

879   Mixed-Phase Clouds in E3SM, Earth and Space Science, 7, e2020EA001125-
880   e002020EA001125, 10.1029/2020EA001125, 2020.

881 Zhang, R., Wang, H., Fu, Q., Pendergrass, A. G., Wang, M., Yang, Y., Ma, P. L., and
882   Rasch, P. J.: Local Radiative Feedbacks Over the Arctic Based on Observed Short-
883   Term Climate Variations, Geophys Res Lett, 45, 5761-5770,
884   10.1029/2018GL077852, 2018.

885 Zhao, C. F., Xie, S. C., Klein, S. A., Protat, A., Shupe, M. D., McFarlane, S. A.,
886   Comstock, J. M., Delanoe, J., Deng, M., Dunn, M., Hogan, R. J., Huang, D., Jensen,
887   M. P., Mace, G. G., McCoy, R., O'Connor, E. J., Turner, D. D., and Wang, Z.:
888   Toward understanding of differences in current cloud retrievals of ARM ground-
889   based measurements, J Geophys Res-Atmos, 117, Artn D10206
890   10.1029/2011jd016792, 2012.

891 Zhao, X., Lin, Y., Peng, Y., Wang, B., Morrison, H., and Gettelman, A.: A single ice
892   approach using varying ice particle properties in global climate model microphysics,
893   Journal of Advances in Modeling Earth Systems, 9, 2138-2157,
894   10.1002/2017MS000952, 2017.

895
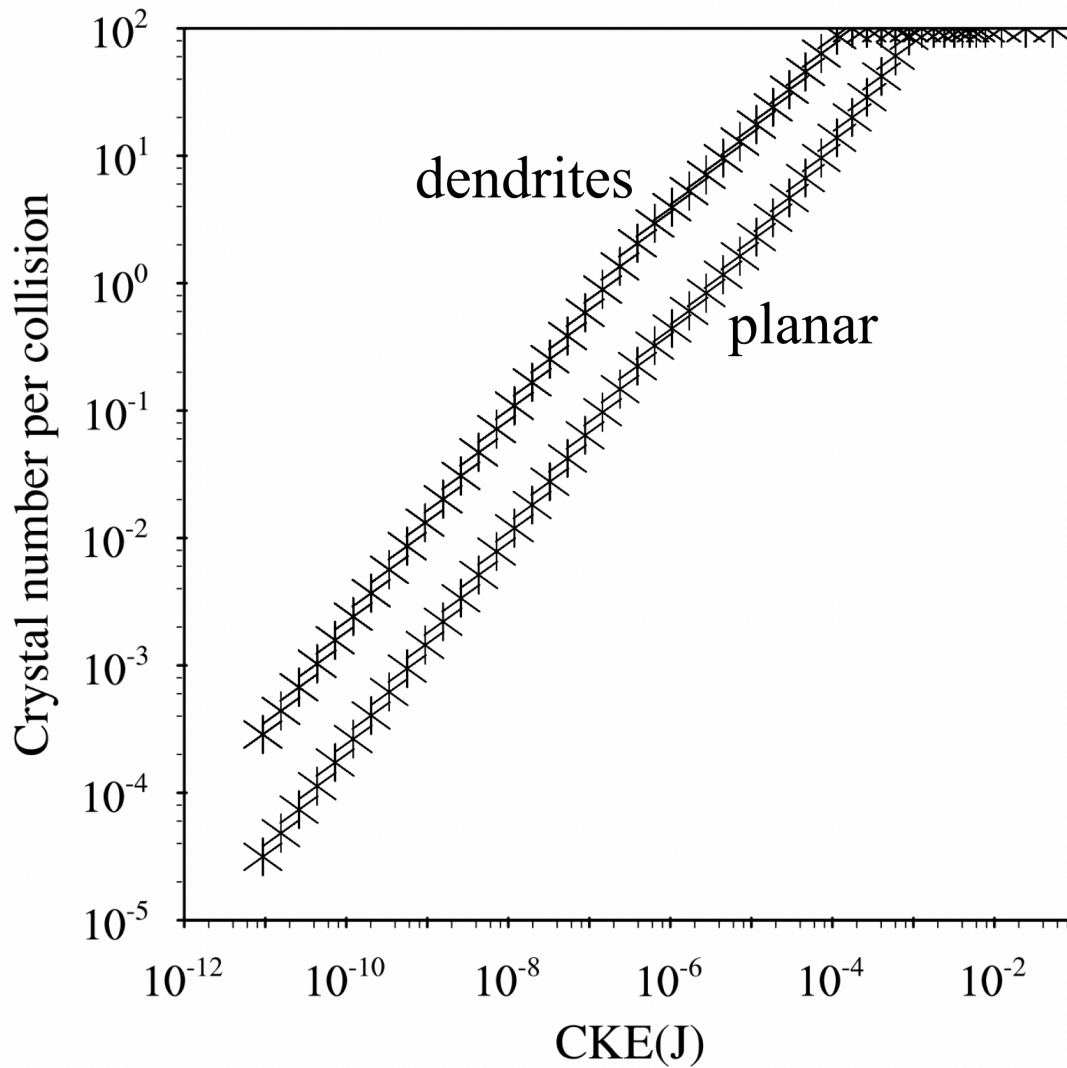
896

897 Figure 1. The number of fragments per collision as a function of initial collisional kinetic

898 energy (CKE). The ice habit is assumed to be dendrites when the temperature (T) is

899 between –12°C and –17°C and is assumed to be spatial planar when –40°C <T<–17°C

900 and –12°C<T<–9°C, following Phillips et al. (2017).

901

902

903
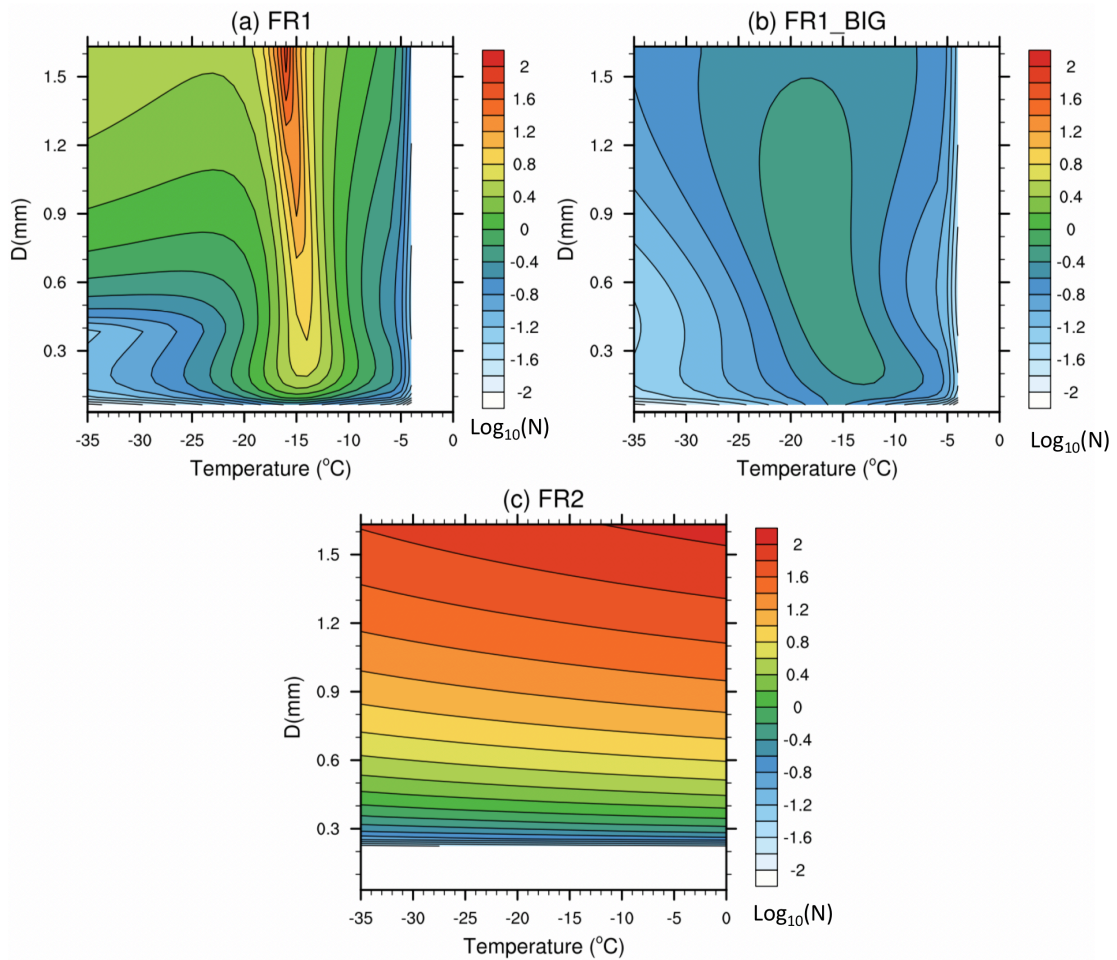
Figure 2. The number of fragments per frozen drop (shown as $\log_{10}N$) as a function of
temperature and particle diameter, from (a) mode 1 of the rain freezing fragmentation
(FR1), (b) mode 1 of the rain freezing fragmentation but for the big fragments
(FR1_BIG), and (c) mode 2 of the rain freezing fragmentation (FR2).
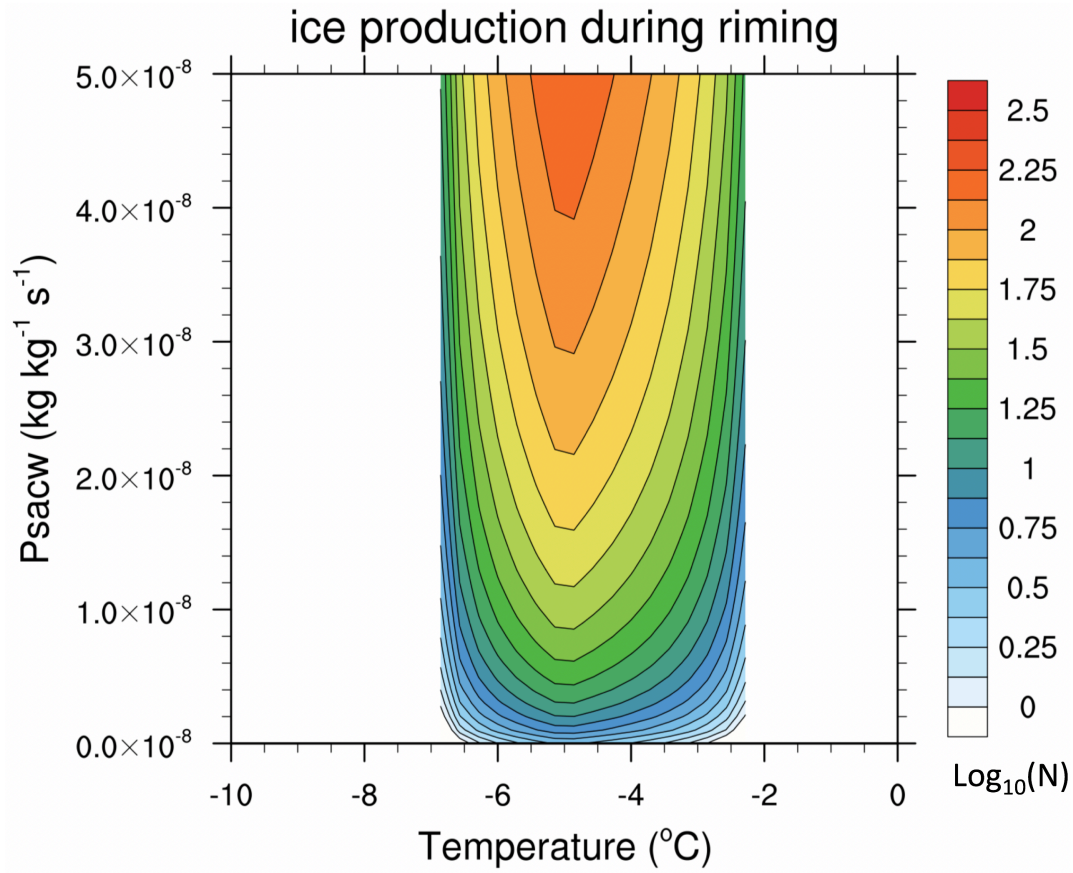
908

909   Figure 3. The rime splintering rate (shown as $\log_{10}N$) as a function of temperature and

910   riming rate.

911
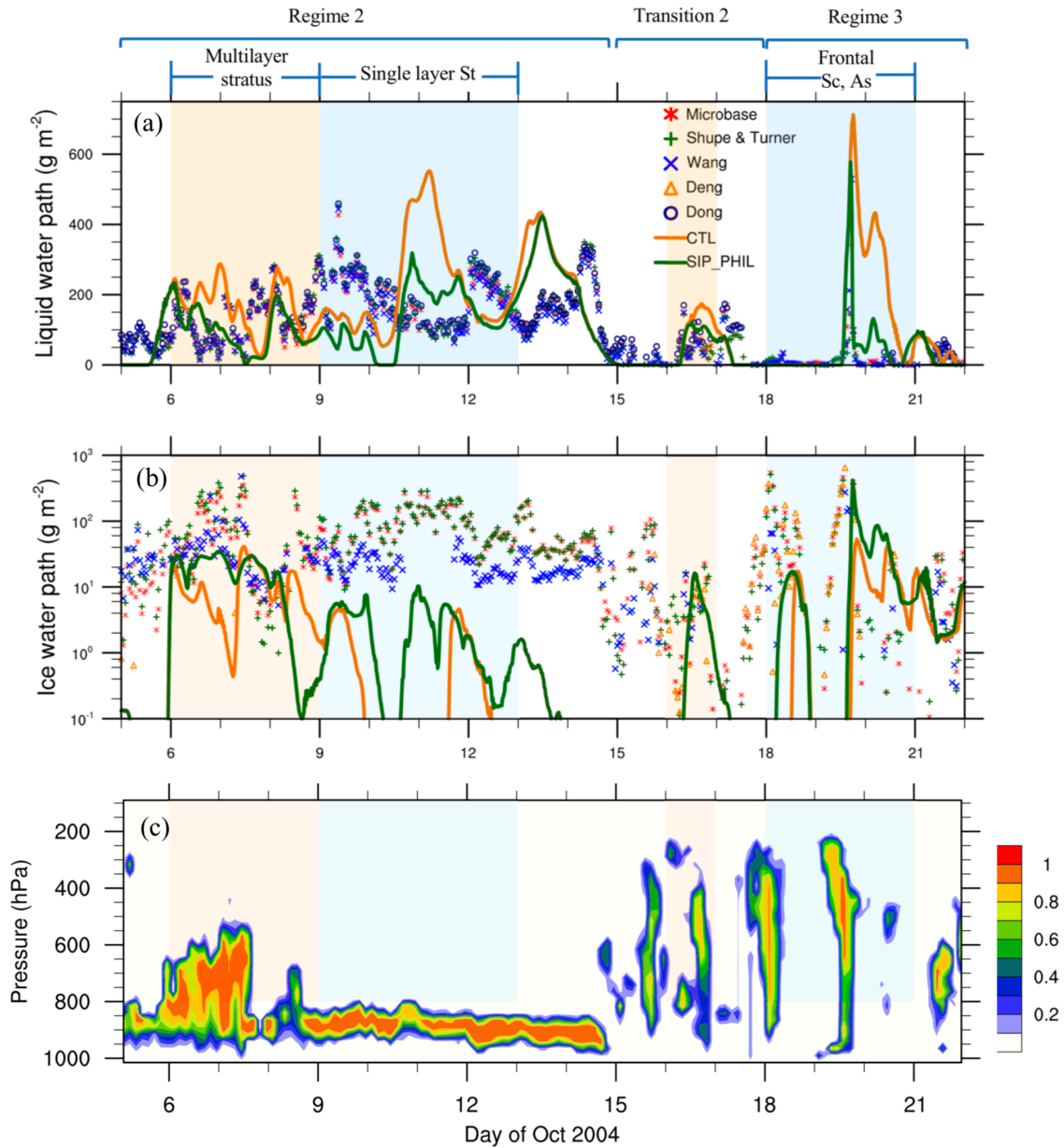
Figure 4. Temporal evolution of (a) LWP, (b) IWP from remote sensing retrievals shown as different markers, CTL experiment (orange solid line) and SIP_PHIL experiment (dark green solid line), and (c) observed time-pressure cross section of the cloud fraction. The shadings show the multilayer stratus, single-layer stratus, transition, and frontal periods.

916
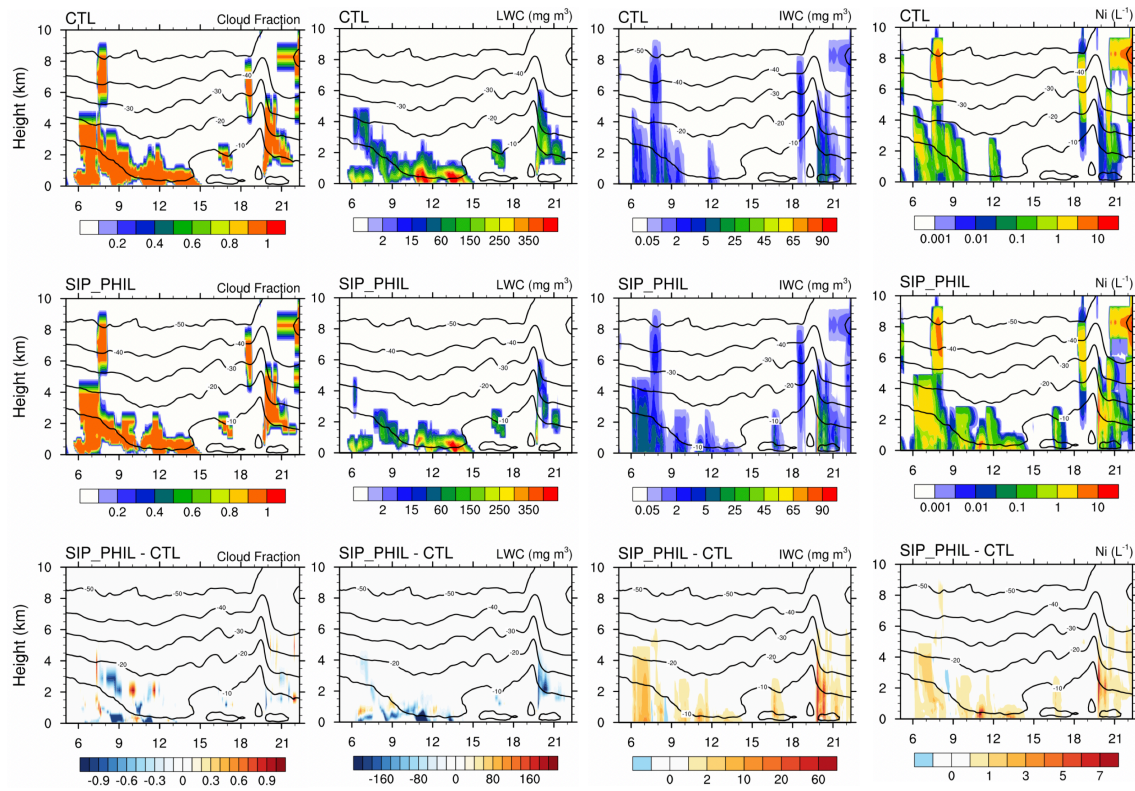
917

918 Figure 5. Time-height cross section of cloud fraction (first column), LWC (second

919 column), IWC (third column) and ice crystal number concentration (fourth column) from

920 CTL (first row), SIP_PHIL (second row) and the differences between SIP_PHIL and

921 CTL (SIP_PHIL minus CTL, third row).

922
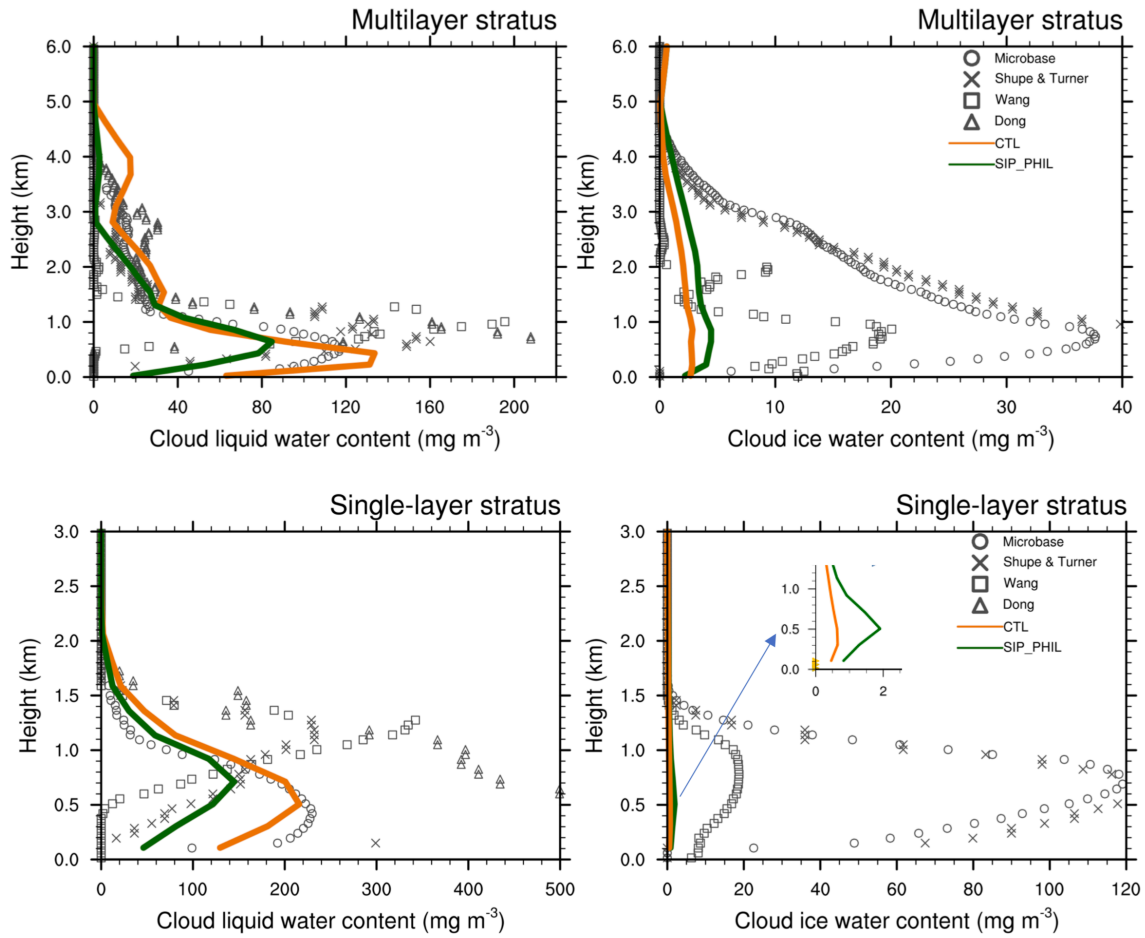
923

924 Figure 6. Vertical profiles of IWC and LWC during multilayer stratus and single-layer

925 stratus periods from remote sensing retrievals shown as different markers, CTL

926 experiment (orange solid line) and SIP_PHIL experiment (dark green solid line).
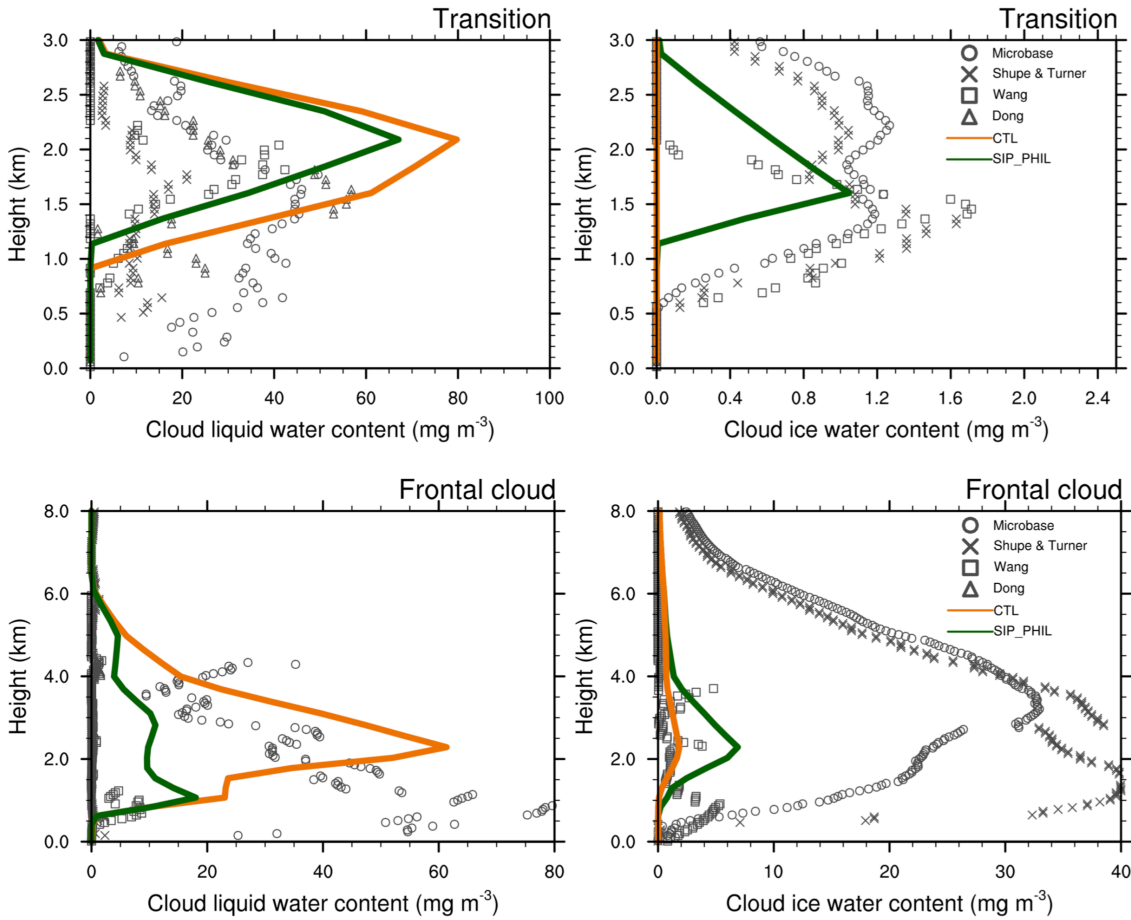
927

928

929 Figure 7. Vertical profiles of IWC and LWC during the transition and frontal cloud

930 periods, from remote sensing retrievals shown as different markers, CTL experiment

931 (orange solid line) and SIP_PHIL experiment (dark green solid line).
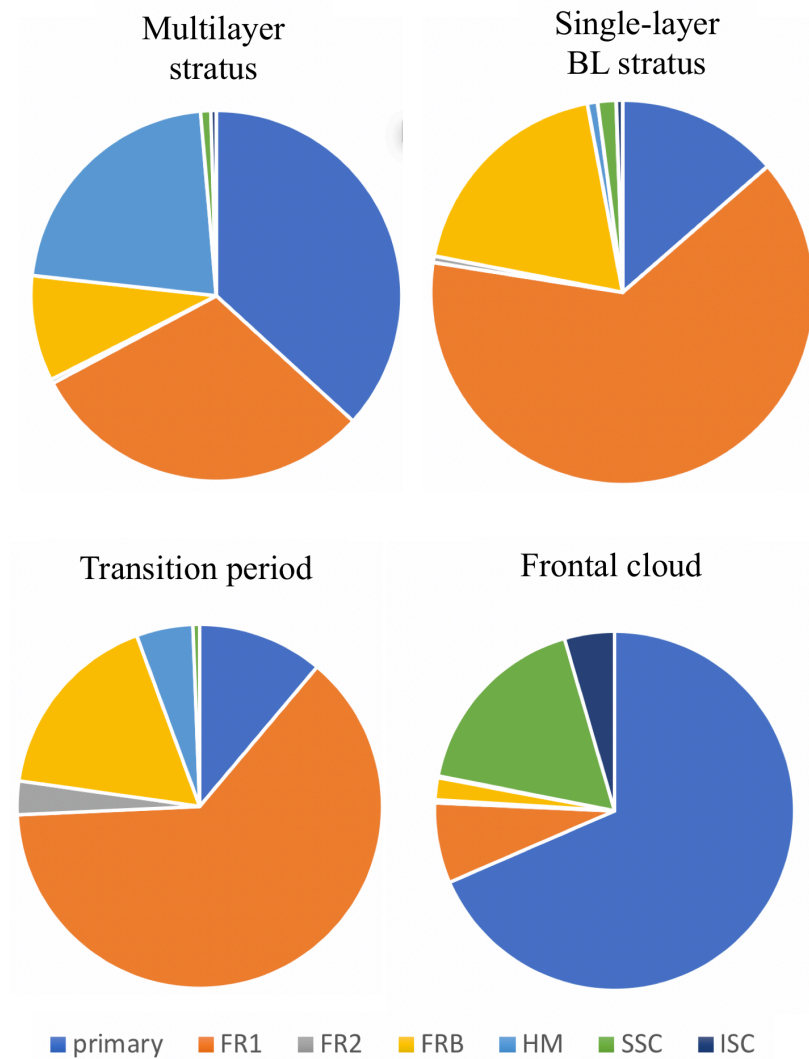
932
Figure 8. Pie charts showing the relative contributions to total ice production from
primary production (i.e., ice nucleation), rime splintering (HM), fragmentation of frozen
rain (including the small fragments in the first mode (FR1), big fragments in the first
mode (FRB), and the second mode (FR2)), breakup from ice–ice collisions (including
snow and cloud ice collision (ISC) and snow and snow collision (SSC)) during the four
M-PACE periods, the vertically integrated process rates are used in the plot.

939
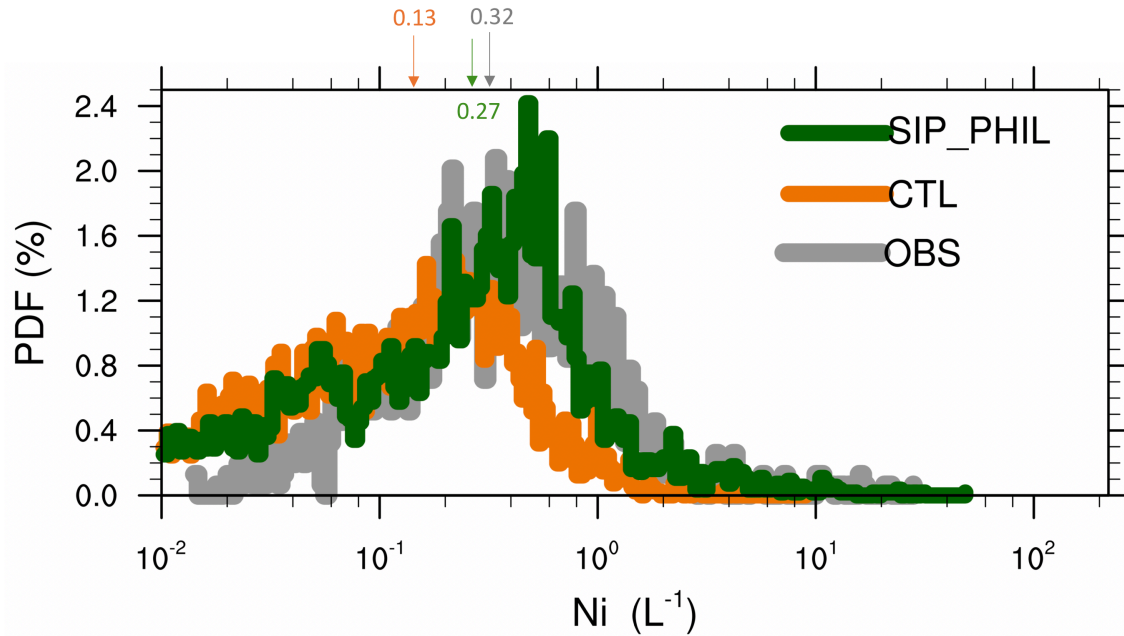
955

956 Figure 11. The probability density function (PDF) of ice crystal number concentrations

957 from observation (gray line), CTL (orange line), and SIP_PHIL simulations (green line).

958 The arrow indicates the median of each distribution which means that the set of values

959 less (or greater) than the median has a probability of 50%. Only ice particles with

960 diameters larger than 100 μm from observations and model simulations are included in

961 the comparison. A correction factor of ¼ is applied to the observed ice number

962 concentrations based on Jackson and McFarquhar (2014) and Jackson et al. (2014).

963

964
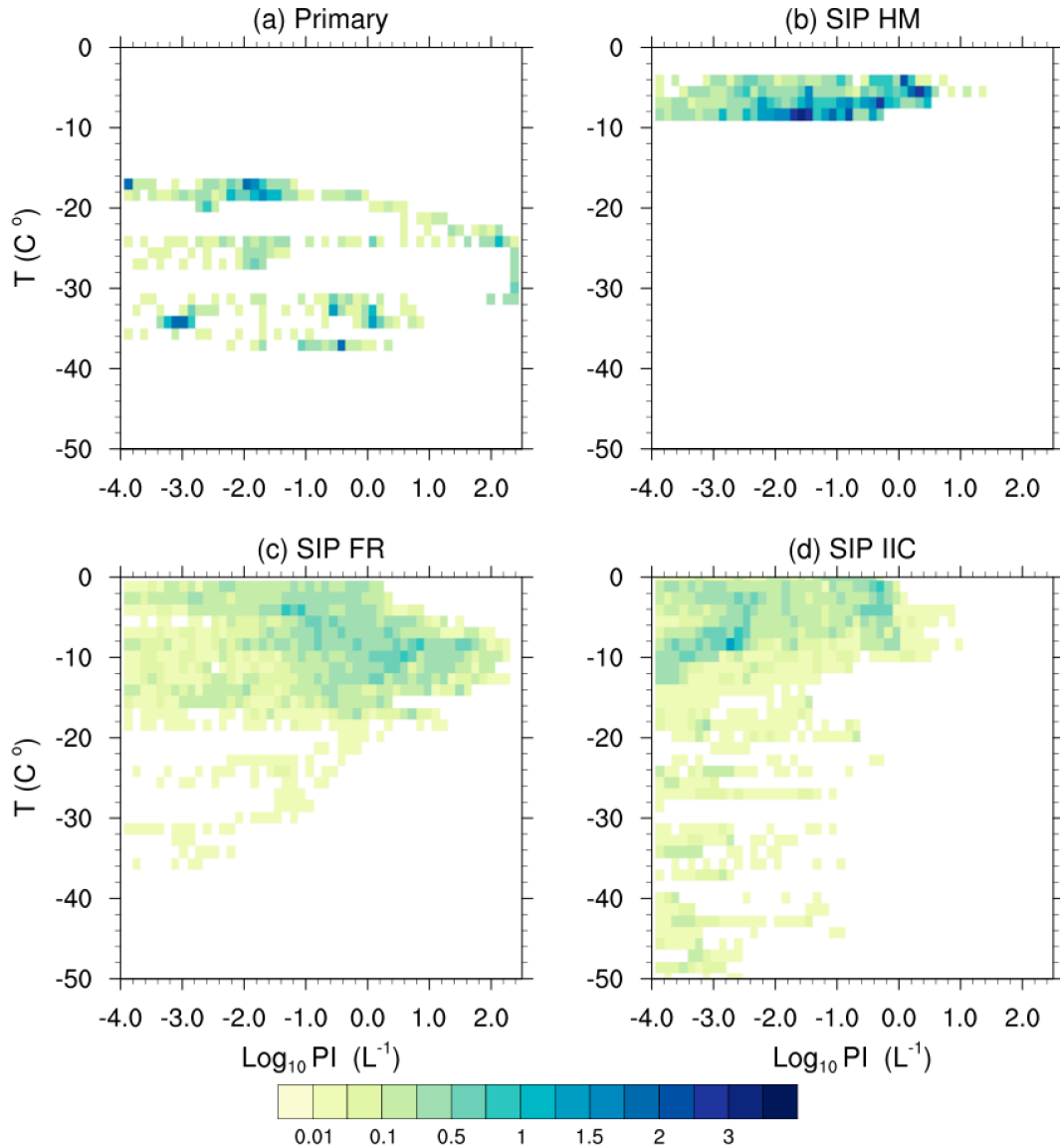
968 Figure 12. Bivariate joint probability density function of ice production defined in terms
969 of temperature and ice production, (a) primary ice production; (b) ice production from
970 riming splintering; (c) ice production from rain fragmentation; (d) ice production from
971 ice-ice collision. The ice production (PI, with unit of # L^{-1}) is calculated as ice production
972 rate ($L^{-1}s^{-1}$) multiplied by model time step (20 mins), shown in Log_{10}.

973

974

975   Table 1. List of experiments.

976

	Type of Secondary ice production	References
CTL	Rime splintering	[Cotton et al., 1986]
SIP_PHIL	Rime splintering	[Cotton et al., 1986]
	Ice-ice collision fragmentation	[Phillips et al., 2017]
	Rain freezing fragmentation	[Phillips et al., 2018]
CTL_no_HM	Same as CTL, but no HM process	

977
978
979
980

981

982 Table 2. The temporally-averaged IWP, LWP (unit: g m^{-2}), and vertically-integrated ice

983 crystal number concentration (unit: m^{-2}) during the four periods from observation, and CTL,

984 CTL_no_HM, and SIP_PHIL experiments.

985

		Multilayer stratus	Single-layer stratus	Transition	Frontal cloud
IWP	OBS	55.6	74.7	5.6	97.0
	CTL	11.2	0.9	0.0001	10.4
	CTL_no_HM	11.1	0.9	0.0001	8.2
	SIP_PHIL	17.1	2.5	3.6	26.1
LWP	OBS	134.4	190.2	58.3	50.2
	CTL	165.1	217.6	88.4	127.6
	CTL_no_HM	166.0	218.0	88.4	129.8
	SIP_PHIL	102.8	131.0	62.1	41.2
ICNC	CTL	5.77×10^6	3.22×10^5	7.66	2.26×10^6
	CTL_no_HM	5.70×10^6	3.17×10^5	0.77	1.57×10^6
	SIP_PHIL	7.09×10^6	1.30×10^6	4.57×10^5	4.67×10^6

986

987

988

989

990 Table 3. Percentage of occurrence of liquid, mixed-phase, and ice clouds during single

991 layer mixed-phase clouds from observation, and CTL, CTL_no_HM, and SIP_PHIL

992 experiments.

993

	Liquid	Mixed-phase	Ice
OBS (%)	16.0	62.7	22.3
CTL (%)	73.0	26.9	0.1
CTL_no_HM (%)	73.0	26.9	0.1
SIP_PHIL (%)	40.8	58.0	1.2

994

995